CHANG-ES – VI. Probing Supernova energy deposition in spiral galaxies through multiwavelength relationships

Jiang-Tao Li,[1]★ Rainer Beck,[2] Ralf-Jürgen Dettmar,[3] George Heald,[4] Judith Irwin,[5] Megan Johnson,[6] Amanda A. Kepley,[7] Marita Krause,[2] E. J. Murphy,[8] Elena Orlando,[9] Richard J. Rand,[10] A. W. Strong,[11] Carlos J. Vargas,[12] Rene Walterbos,[12] Q. Daniel Wang[13] and Theresa Wiegert[5]

[1]*Department of Astronomy, University of Michigan, 311 West Hall, 1085 S. University Ave, Ann Arbor, MI 48109-1107, USA*
[2]*Max-Planck-Institut für Radioastronomie, Auf dem Hügel 69, D-53121 Bonn, Germany*
[3]*Astronomisches Institut, Ruhr-Universität Bochum, D-44780 Bochum, Germany*
[4]*Netherlands Institute for Radio Astronomy (ASTRON), Postbus 2, NL-7990 AA Dwingeloo, the Netherlands*
[5]*Department of Physics, Engineering Physics & Astronomy, Queen's University, Kingston, ON K7L 3N6, Canada*
[6]*CSIRO, PO Box 76, Epping, NSW 1710, Australia*
[7]*National Radio Astronomy Observatory, 520 Edgemont Road, Charlottesville, VA 22903-2475, USA*
[8]*Observatories of the Carnegie Institution for Science, 813 Santa Barbara Street, Pasadena, CA 91101, USA*
[9]*Physics/Astrophysics Building, 452 Lomita Mall, Stanford University, Stanford, CA 94305-4085, USA*
[10]*Department of Physics and Astronomy, University of New Mexico, 800 Yale Boulevard, NE, Albuquerque, NM 87131, USA*
[11]*Max-Planck-Institut für extraterrestrische Physik, D-85741 Garching bei München, Germany*
[12]*Department of Astronomy, New Mexico State University, PO Box 30001, MSC 4500, Las Cruces, NM 88003, USA*
[13]*Department of Astronomy, University of Massachusetts, 710 North Pleasant St, Amherst, MA 01003, USA*

ABSTRACT

How a galaxy regulates its supernovae (SNe) energy into different interstellar/circumgalactic medium components strongly affects galaxy evolution. Based on the *JVLA* D-configuration C- (6 GHz) and *L*-band (1.6 GHz) continuum observations, we perform statistical analysis comparing multiwavelength properties of the Continuum Haloes in Nearby Galaxies – an *EVLA* Survey galaxies. The high-quality *JVLA* data and edge-on orientation enable us for the first time to include the halo into the energy budget for a complete radio-flux-limited sample. We find tight correlations of $L_{\rm radio}$ with the mid-IR-based star formation rate (SFR). The normalization of our $I_{\rm 1.6\,GHz}/{\rm W\,Hz^{-1}}$–SFR relation is ∼2–3 times of those obtained for face-on galaxies, probably a result of enhanced IR extinction at high inclination. We also find tight correlations between $L_{\rm radio}$ and the SNe energy injection rate $\dot{E}_{\rm SN(Ia+CC)}$, indicating the energy loss via synchrotron radio continuum accounts for ∼1 of $\dot{E}_{\rm SN}$, comparable to the energy contained in cosmic ray electrons. The integrated *C*-to-*L*-band spectral index is $\alpha \sim 0.5$–1.1 for non-active galactic nucleus galaxies, indicating a dominance by the diffuse synchrotron component. The low-scatter $L_{\rm radio}$–SFR/$L_{\rm radio}$-$\dot{E}_{\rm SN(Ia+CC)}$ relationships have superlinear logarithmic slopes at ∼2σ in *L* band ($1.132 \pm 0.067/1.175 \pm 0.102$) while consistent with linear in *C* band ($1.057 \pm 0.075/1.100 \pm 0.123$). The superlinearity could be naturally reproduced with non-calorimeter models for galaxy discs. Using *Chandra* halo X-ray measurements, we find sublinear $L_{\rm X}$–$L_{\rm radio}$ relations. These results indicate that the observed radio halo of a starburst galaxy is close to electron calorimeter, and a galaxy with higher SFR tends to distribute an increased fraction of SNe energy into radio emission (than X-ray).

Key words: galaxies: haloes – galaxies: spiral – galaxies: statistics – infrared: galaxies – radio continuum: galaxies – X-rays: galaxies.

★ E-mail: pandataotao@gmail.com

1 INTRODUCTION

The energetic feedback from supernovae (SNe) and massive stellar winds are crucial in setting the basic properties of galaxies, including masses, sizes, and star formation histories, as studied in numerical and semi-analytical models (e.g. Somerville & Davé 2015 and references therein). In particular, this stellar feedback is thought to be the most important energy source for the multiphase circumgalactic medium (CGM) around galaxies without an active galactic nucleus (AGN). The CGM is comprised of multiphase gas (hot gas $\gtrsim 10^6$ K, e.g. Li & Wang 2013a; warm-hot intergalactic medium $\sim 10^{5\text{-}6}$ K, e.g.Werk et al. 2013; cool gas $\sim 10^{3\text{-}5}$ K, e.g. Hoopes, Walterbos & Rand 1999; and cold gas $< 10^3$ K, e.g. Heald et al. 2011) as well as relativistic particles (cosmic rays; CRs) and magnetic fields (e.g. Krause 2011), which produce broad-band emission via various emitting mechanisms. Until now, how the galaxies distribute their feedback energy into different interstellar medium (ISM) or CGM phases is still poorly understood (e.g. see Wang 2010; Strong et al. 2010 and references therein).

Both the diffuse radio and X-ray emission in and around galaxies are thought to be closely related to SNe feedback. The radio continuum emission at GHz frequencies is mainly produced by the synchrotron energy loss of relativistic electrons at $\sim$GeV energy. These high-energy electrons could be accelerated in SN remnants (SNRs) or superbubbles (e.g. Parizot et al. 2004; Parizot 2014), or from the interaction between the CRs and the ISM (secondary CRs, e.g. Strong, Moskalenko & Ptuskin 2007). On the other hand, the soft X-ray emission at $\sim$0.5-2 keV from galactic haloes is thought to be produced by a hot ($kT \gtrsim 10^7$ K) tenuous ($n \lesssim 10^{-(3\text{-}4)}$ cm^{-3}) galactic outflow and its interface with entrained cool cloudlets, instead of the outflow itself (e.g. Strickland et al. 2002; Strickland & Heckman 2007; Li et al. 2009; Li & Wang 2013b; Zhang et al. 2014; Li 2015). Therefore, the total soft X-ray luminosity is related to both the energy and mass injection rates into the hot phase (e.g. Chevalier & Clegg 1985; Strickland & Stevens 2000; Li et al. 2011; Zhang et al. 2014). As the SN rate and the energy/mass injection rates are all proportional to the star formation rate (SFR) of a galaxy, it is natural that the radio and soft X-ray luminosities of the galactic haloes are both correlated to the mid- or far-infrared (IR) luminosity of the galaxy tracing the star formation activity. However, it is still not clear how the diffuse radio and X-ray luminosities of galaxies depend on the SNe feedback energy injection rate (linear dependence or not), and if the radiation efficiency (the fraction of SN energy converted to radiation) in radio and X-ray stays constant at different SFRs or in different types of galaxies (e.g. Li & Wang 2013b). These questions are fundamental for understanding the fate of mass and energy originated from stellar feedback and its role in regulating the structure and evolution of galaxies.

Tight correlations between radio and IR luminosities of nearby galaxies were discovered as early as the 1980s (e.g. Dickey & Salpeter 1984; de Jong et al. 1985; Helou, Soifer & Rowan-Robinson 1985). In most of the studies, the slope of the L_{radio}–L_{IR} relation is found to be close to linear for the global properties of the galaxies (e.g. Helou et al. 1985; Yun, Reddy & Condon 2001; Vlahakis, Eales & Dunne 2007), but the relation shows clear variations at small scales (e.g. $\sim$kpc; Murphy et al. 2006, 2008; Heesen et al. 2014). Völk (1989) developed a calorimeter theory to explain the tight correlation between the non-thermal radio and thermal IR emission, assuming that the source strengths of relativistic electrons and UV photons are both proportional to the SN rate, and the leptonic CRs (electrons and positrons) lose most of their energy

within the galactic halo, which is also optically thick to the UV photons heating the dust and producing the IR emission. However, it is widely believed that galaxy discs are not calorimeters even for CR electrons, because many galaxies host extended radio haloes (e.g. Krause 2011; Irwin et al. 2013b; Mora & Krause 2013). On the other hand, whether or not a galactic halo can be assumed to be a calorimeter for CR electrons is quite uncertain, and could be affected by many factors (e.g. Strong et al. 2010). We therefore need to consider the radio halo in the total SNe feedback energy budget. Slightly but significantly non-linear L_{radio}–L_{IR} relations have also been found and non-calorimeter models have been developed to explain them (e.g. Chi & Wolfendale 1990; Price & Duric 1992; Xu et al. 1994; Niklas 1997; Niklas & Beck 1997; Bell 2003; Lacki, Thompson & Quataert 2010; Irwin et al. 2013b; Basu et al. 2015b). These studies are extremely important for small scales (e.g. $\sim$kpc) or low-SFR galaxies which do not match the calorimeter conditions.

'Continuum Haloes in Nearby Galaxies – an *EVLA* Survey' (CHANG-ES; Irwin et al. 2012a) is an unprecedented deep radio continuum survey of a radio-flux-limited sample of 35 nearby edge-on spiral galaxies with the Karl G. Jansky Very Large Array (hereafter *JVLA*) in its commissioning phase. For the first time, the deep *JVLA* observations enable us to detect radio continuum haloes in a statistically meaningful sample of nearby galaxies, thus allowing CRs and magnetic fields in the halo to be included in the energy budget of galactic feedback. The major goals of the CHANG-ES project are to investigate the occurrence, origin, and nature of the radio continuum haloes, and to probe the disc–halo interaction. A descriptions of the full project is presented in detail in Irwin et al. (2012a, Paper I). Detailed case studies of three galaxies, NGC 4631, UGC 10288, and NGC 4845, are presented in Irwin et al. (2012b, Paper II), Irwin et al. (2013a, Paper III), and Irwin et al. (2015, Paper V), respectively.

In Paper IV (Wiegert et al. 2015), we presented intensity maps in two frequency bands [C (6 GHz) and L (1.6 GHz)], with different weightings, as well as in-band spectral index maps, polarization maps, and spatially resolved mid-IR measurements of the SFRs. The data products are available to the public in CHANG-ES Data Release 1 at http://www.queensu.ca/changes. Our early results in Paper IV indicate that a galaxy with a higher SFR surface density tends to host a larger halo of magnetic fields and CRs. As presented in Paper IV, the D-configuration measurements in *C* and *L* bands of the whole sample have little missing flux, therefore they are well suited for statistical analysis of the total radio continuum luminosity of the galaxies. Furthermore, 16 of the 35 CHANG-ES sample galaxies are also included in the *Chandra* survey of nearby highly inclined disc galaxies by Li & Wang (2013a,b) and Li, Crain & Wang (2014). The *JVLA* and *Chandra* measurements enable us to directly compare the diffuse radio and X-ray emission from both the galactic disc and halo, which are thought to be related to two of the most energetic phases of galactic feedback: the CR and the hot galactic outflow.

In this paper, we present statistical analysis of the radio continuum and soft X-ray emission of the CHANG-ES galaxies based on the *JVLA* D-configuration and the *Chandra* observations. The paper is organized as follows: In Section 2, we summarize the data and galaxy parameters used in this paper and define some subsamples. In Section 3, we present a statistical analysis of the radio continuum emission of the galaxies and compare it to the X-ray and multiwavelength properties of the galaxies. We further discuss the scientific implications of this statistical analysis in Section 4. Our major results and conclusions are summarized in Section 5.

Table 1. Parameters of the CHANG-ES Galaxies. Parameters of the CHANG-ES sample galaxies, those marked with * are included in the *Chandra* sample of nearby edge-on disc galaxies (Li & Wang 2013a,b; Li et al. 2014). *d* is the distance obtained from Irwin et al. (2012a) and further updated in Wiegert et al. (2015). TC is the morphological type code. *B*−*V* is the *B*−*V* band colour corrected for galactic extinction, inclination, and redshift. v_{rot} is the maximum gas rotation velocity corrected for inclination. TC, *B*−*V*, and v_{rot} are obtained from the HyperLeda data base (Makarov et al. 2014; http://leda.univ-lyon1.fr/). M_{TF} is the total baryon mass estimated from v_{rot} using the *K*-band baryonic Tully–Fisher relation (Bell & de Jong 2001). M_* is the stellar mass, estimated from the *2MASS K*-band apparent magnitude (Skrutskie et al. 2006), the distance, and the *B*−*V* colour, adopting a colour-dependent stellar mass-to-light ratio (Bell & de Jong 2001). $\dot{E}_{SN,CC}$ and $\dot{E}_{SN,Ia}$ are the CC and Type Ia SNe energy injection rate estimated from the SFR (from Wiegert et al. 2015) and M_*, adopting the CC and Type Ia SN rate from Heckman et al. (1990) and Mannucci et al. (2005), respectively. $L_{6\,GHz}$ and $L_{1.6\,GHz}$ are the *C*-band and *L*-band luminosities, estimated by adopting a bandwidth of 2 GHz and 500 MHz in *C* and *L* bands, respectively. The relatively large error of UGC 10288 is caused by a strong background source (Irwin et al. 2013a). α is the integrated spectral index between *C* and *L* bands of the whole galaxy. 'RF', 'RB', 'ERB' in the 'AGN' column denote radio faint, radio bright, and extremely radio bright. Only ERB AGN could significantly affect the radio flux measurement.

Galaxy	d (Mpc)	TC	$B{-}V$ (mag)	v_{rot} (km s^{-1})	M_{TF} ($\times 10^{10}$M$_\odot$)	M_* ($\times 10^{10}$M$_\odot$)	$\dot{E}_{SN,CC}$ ($\times 10^{41}$ergs s^{-1})	$\dot{E}_{SN,Ia}$ ($\times 10^{41}$ergs s^{-1})	$L_{6\,GHz}$ ($\times 10^{38}$ergs s^{-1})	$L_{1.6\,GHz}$ ($\times 10^{38}$ergs s^{-1})	α	AGN
NGC660*	12.3	1.3 ± 1.2	0.71	141.4	2.08	2.10 ± 0.03	6.69 ± 0.13	0.293 ± 0.004	2.382 ± 0.048	0.476 ± 0.010	−0.17 ± 0.02	ERB
NGC891*	9.1	3.1 ± 0.4	0.70	212.1	8.63	4.13 ± 0.06	3.78 ± 0.08	0.575 ± 0.008	0.414 ± 0.014	0.369 ± 0.007	0.95 ± 0.03	RF
NGC2613	23.4	3.1 ± 0.5	0.70	290.6	26.08	11.96 ± 0.19	4.22 ± 0.08	0.201 ± 0.004	0.195 ± 0.008	1.02 ± 0.03	RF
NGC2683	6.3	3.0 ± 0.3	0.75	202.6	7.35	1.49 ± 0.02	0.220 ± 0.004	0.207 ± 0.003	0.019 ± 0.001	0.016 ± 0.002	0.89 ± 0.08	RF
NGC2820	26.5	5.3 ± 0.6	0.23	162.8	3.41	0.467 ± 0.013	1.51 ± 0.03	0.065 ± 0.002	0.321 ± 0.007	0.259 ± 0.005	0.88 ± 0.02	RF
NGC2992	34.0	0.9 ± 0.5	0.77	58.7	0.10	5.26 ± 0.09	7.86 ± 0.24	0.734 ± 0.012	2.225 ± 0.044	1.417 ± 0.028	0.70 ± 0.02	ERB
NGC3003	25.4	4.3 ± 0.8	0.28	120.6	1.19	0.485 ± 0.010	1.63 ± 0.03	0.068 ± 0.001	0.167 ± 0.008	0.135 ± 0.003	0.88 ± 0.04	RF
NGC3044	20.3	5.5 ± 0.7	0.35	152.6	2.72	0.660 ± 0.013	2.32 ± 0.05	0.092 ± 0.002	0.370 ± 0.009	0.257 ± 0.005	0.76 ± 0.02	RF
NGC3079*	20.6	6.6 ± 0.9	0.53	208.4	8.11	4.73 ± 0.07	8.44 ± 0.17	0.660 ± 0.010	3.711 ± 0.074	2.059 ± 0.041	0.60 ± 0.02	ERB
NGC3432	9.4	8.9 ± 0.5	0.29	109.9	0.86	0.100 ± 0.002	0.366 ± 0.007	0.0140 ± 0.0003	0.056 ± 0.001	0.044 ± 0.001	0.86 ± 0.02	RF
NGC3448	24.5	1.8 ± 2.5	0.31	119.5	1.15	0.564 ± 0.011	2.24 ± 0.04	0.079 ± 0.002	0.295 ± 0.006	0.165 ± 0.003	0.60 ± 0.02	RF
NGC3556*	14.1	6.0 ± 0.3	0.57	153.2	2.76	2.81 ± 0.04	5.29 ± 0.11	0.392 ± 0.006	0.376 ± 0.022	0.346 ± 0.007	0.97 ± 0.05	RF
NGC3628*	8.5	3.1 ± 0.4	0.68	215.4	9.11	2.83 ± 0.04	2.46 ± 0.05	0.394 ± 0.006	0.319 ± 0.006	0.228 ± 0.005	0.78 ± 0.02	RB
NGC3735	42.0	5.3 ± 0.6	0.00	241.1	13.55	14.92 ± 0.21	2.68 ± 0.05	2.08 ± 0.03	1.051 ± 0.021	0.858 ± 0.017	0.88 ± 0.02	RF
NGC3877*	17.7	5.1 ± 0.5	0.65	155.1	2.87	2.74 ± 0.04	2.24 ± 0.04	0.382 ± 0.006	0.097 ± 0.002	0.080 ± 0.002	0.89 ± 0.02	RF
NGC4013*	16.0	3.1 ± 0.5	0.83	181.4	4.99	3.23 ± 0.05	1.17 ± 0.02	0.450 ± 0.007	0.077 ± 0.002	0.058 ± 0.001	0.82 ± 0.02	RB
NGC4096	10.3	5.3 ± 0.6	0.50	144.8	2.26	0.613 ± 0.010	0.659 ± 0.013	0.086 ± 0.001	0.042 ± 0.001	0.036 ± 0.001	0.94 ± 0.02	RF
NGC4157	15.6	3.3 ± 0.7	0.64	188.9	5.75	2.92 ± 0.04	3.05 ± 0.06	0.407 ± 0.006	0.321 ± 0.006	0.269 ± 0.005	0.90 ± 0.02	RF
NGC4192	13.6	2.6 ± 0.8	0.66	214.8	9.03	3.40 ± 0.05	1.37 ± 0.03	0.474 ± 0.007	0.107 ± 0.002	0.089 ± 0.002	0.89 ± 0.02	RF
NGC4217*	20.6	3.1 ± 0.4	0.75	187.6	5.62	4.74 ± 0.07	3.73 ± 0.07	0.661 ± 0.010	0.360 ± 0.007	0.283 ± 0.006	0.86 ± 0.02	RF
NGC4244*	4.4	5.9 ± 0.6	0.41	97.8	0.57	0.090 ± 0.002	0.049 ± 0.001	0.0125 ± 0.0003	0.0042 ± 0.0003	0.0021 ± 0.0001	0.52 ± 0.06	RF
NGC4302	19.4	5.4 ± 0.7	0.74	167.4	3.76	3.43 ± 0.05	1.29 ± 0.03	0.478 ± 0.007	0.108 ± 0.003	0.102 ± 0.002	0.99 ± 0.02	RB
NGC4388*	16.6	2.8 ± 0.6	0.57	171.2	4.07	1.54 ± 0.02	0.171 ± 0.003	0.215 ± 0.003	0.410 ± 0.008	0.216 ± 0.004	0.56 ± 0.02	ERB
NGC4438*	10.4	0.6 ± 1.3	0.76	167.3	3.76	1.63 ± 0.02	0.171 ± 0.005	0.228 ± 0.003	0.141 ± 0.003	0.085 ± 0.002	0.66 ± 0.02	ERB
NGC4565*	11.9	3.3 ± 0.7	0.68	244.3	14.18	6.04 ± 0.08	1.81 ± 0.04	0.842 ± 0.012	0.143 ± 0.004	0.129 ± 0.003	0.96 ± 0.02	RB
NGC4594	12.7	1.1 ± 0.3	0.88	408.0	85.82	26.12 ± 0.36	0.781 ± 0.016	3.64 ± 0.05	0.495 ± 0.010	0.090 ± 0.002	−0.24 ± 0.02	ERB
NGC4631*	7.4	6.6 ± 0.7	0.39	138.4	1.93	0.960 ± 0.015	3.25 ± 0.06	0.134 ± 0.002	0.373 ± 0.010	0.355 ± 0.012	1.00 ± 0.03	RF
NGC4666*	27.5	5.1 ± 0.7	0.64	192.9	6.19	12.48 ± 0.18	17.79 ± 0.36	1.74 ± 0.03	2.268 ± 0.045	1.830 ± 0.037	0.88 ± 0.02	RF
NGC4845	17.0	2.3 ± 0.8	0.78	176.0	4.48	2.89 ± 0.05	1.17 ± 0.02	0.403 ± 0.007	2.981 ± 0.059	0.397 ± 0.008	−0.47 ± 0.02	ERB
NGC5084	23.4	−2.0 ± 0.4	0.93	312.9	33.81	12.33 ± 0.19	0.244 ± 0.012	1.72 ± 0.03	0.473 ± 0.013	0.133 ± 0.003	0.09 ± 0.03	ERB
NGC5297	40.4	4.9 ± 0.7	0.50	189.5	5.81	3.69 ± 0.07	3.10 ± 0.06	0.515 ± 0.009	0.262 ± 0.016	0.238 ± 0.005	0.96 ± 0.05	RF
NGC5775*	28.9	5.2 ± 0.6	0.66	187.2	5.57	7.72 ± 0.10	12.88 ± 0.26	1.08 ± 0.01	1.487 ± 0.030	1.274 ± 0.025	0.92 ± 0.02	RF
NGC5792	31.7	3.0 ± 0.3	0.69	208.6	8.15	8.89 ± 0.16	6.42 ± 0.13	1.24 ± 0.02	0.486 ± 0.010	0.347 ± 0.007	0.78 ± 0.02	RB
NGC5907	16.8	5.3 ± 0.6	0.62	226.6	10.89	5.82 ± 0.09	3.81 ± 0.08	0.812 ± 0.012	0.348 ± 0.007	0.307 ± 0.006	0.94 ± 0.02	RF
UGC10288	34.1	5.3 ± 0.6	0.66	167.1	3.74	2.03 ± 0.05	1.00 ± 0.03	0.284 ± 0.007	0.043 ± 0.001	0.031 ± 0.003	0.79 ± 0.09	RF

2 GALAXY PARAMETERS AND SUBSAMPLE DEFINITION

2.1 Galaxy parameters

In this paper, we study the dependence of the diffuse radio continuum luminosity of the whole galaxy (disc+halo, L_{radio}) on the multiwavelength properties of the galaxies, such as the SFR and the SFR surface density, the stellar mass (M_*), the total baryon mass (M_{TF}), and the energy injection rate from core-collapsed (CC) and Type Ia SNe ($\dot{E}_{SN,CC}$ and $\dot{E}_{SN,Ia}$). We list these parameters, as well as some other related parameters of the CHANG-ES galaxies, in Table 1. More information about the sample galaxies is summarized in Irwin et al. (2012a) and Wiegert et al. (2015).

The SFR and the SFR surface density (Σ_{SFR}) are directly quoted from Wiegert et al. (2015) (Fig. 1a, but *not* listed in Table 1). These star formation parameters are measured with spatially resolved *WISE* 22 μm images, after removing bright unresolved nuclear sources in NGC 3735 and NGC 4388, which are assumed to be due to an AGN. The *WISE* 22 μm SFRs adopted in Paper IV and this paper are systematically lower than those adopted in Paper I (on average 2.74 times lower). This is partially because in Paper I we have adopted an old SFR calibrator from Kennicutt (1998) which gives a SFR ∼17 per cent higher than the recent result (Kennicutt & Evans 2012), and partially because the SFR based on total IR luminosity (as adopted in Paper I) is also systematically higher than that based on mid-IR luminosity (e.g. *WISE* 22 μm or *Spitzer* 24 μm; Rieke et al. 2009; Calzetti et al. 2010). In addition, the average total IR to mid-IR luminosity ratio of our sample is ∼(18–60) per cent
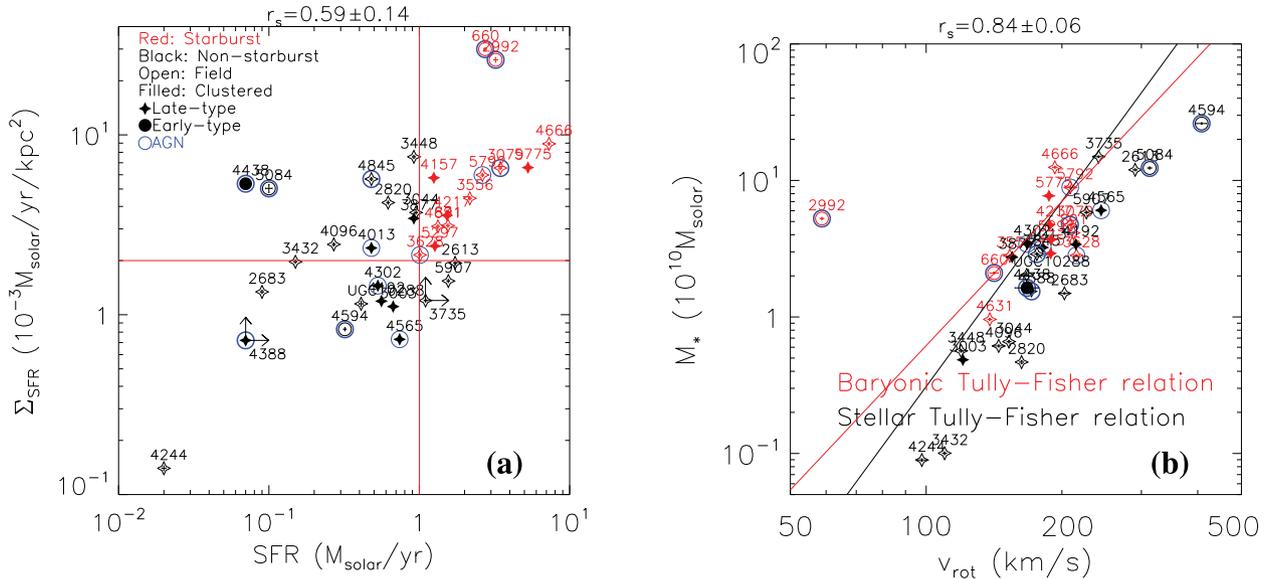
Figure 1. Basic properties of the CHANG-ES galaxies. (a) The SFR and the SFR surface density (Σ_{SFR}). Different subsamples are plotted with different symbols: starburst (red) versus non-starburst (black); field (open) versus clustered (filled); late-type (diamond) versus early-type (circle). Symbols for galaxies hosting a RB AGN which could highly affect the radio flux density measurements are surrounded with a thick blue circle, while those with an AGN but unlikely to strongly affect the radio flux measurements are marked with a thin blue circle ('ERB' and 'RB' in the last column of Table 1, respectively). Data points of NGC 3735 and NGC 4388 are lower limits after removing the AGN (Wiegert et al. 2015). The two red lines at SFR = 1 M$_\odot$ yr^{-1} and SFR surface density = 2×10^{-3} M$_\odot$ yr^{-1} kpc^{-2} separate starburst and non-starburst galaxies (Section 2.2). The correlation coefficient r_s (Section 3) is calculated for the whole sample. (b) The stellar mass (M_*) and gas rotation velocity (v_{rot}). v_{rot} is used to derive the baryonic mass of the galaxies adopting the baryonic Tully–Fisher relation from Bell & de Jong (2001, shown as a red solid line). We also plot the stellar Tully–Fisher relation from Bell & de Jong (2001) for comparison (the black solid line). The correlation coefficient r_s is calculated after removing the interacting galaxy NGC 2992.

higher than those in the literature (e.g. Rieke et al. 2009; Calzetti et al. 2010), which could be an effect of the strong extinction in our highly inclined galaxies. We caution that each star formation tracer has its biases. We herein choose the *WISE* 22 μm luminosity as the star formation tracer because it is less affected by the cold dust heated by the general interstellar radiation field which is not related to current star formation. This cold dust contribution could be important for low-SFR galaxies (e.g. Temi, Brighenti & Mathews 2009), which are common in our sample.

We estimate M_* of the galaxies using the *2MASS* K-band magnitude (Skrutskie et al. 2006) and a colour-dependent mass-to-light ratio from Bell & de Jong (2001). This estimate shows no significant difference from recent estimates of the stellar mass based on *Spitzer* (Zhu et al. 2010) or *WISE* observations (Jarrett et al. 2013). For NGC 3735, which does not have an extinction-corrected $B-V$ colour listed in the HyperLeda data base (Makarov et al. 2014), we assume the mass-to-light ratio to be 1.

We estimate M_{TF} from the inclination-corrected maximum gas rotation velocity (v_{rot}) and the baryonic Tully–Fisher relation (Fig. 1b). M_{TF} includes the contribution from stars and the H$_I$ gas, but does not include the contribution from molecular gas (Bell & de Jong 2001). Since M_{TF} is derived from the rotation velocity, it provides an alternative distance-independent measurement of the galaxy mass to those derived from the photometry methods (such as M_*, which depends on the assumed distance).

Both the radio continuum and X-ray emission of galaxies are thought to be closely related to SN feedback. However, SNe could be produced by both young and old stellar populations, which are quite different in both temporal and spatial distributions. We therefore need to estimate the energy injection rate from CC and Type Ia SNe, which are related to young and old stellar populations, respectively, in order to quantitatively combine the contributions

from both populations (e.g. Li & Wang 2013b). We estimate $\dot{E}_{SN,CC}$ and $\dot{E}_{SN,Ia}$, adopting the CC SN rate per unit SFR from Heckman, Armus & Miley (1990) and the Type Ia SN rate per unit stellar mass from Mannucci et al. (2005). We also assume each SN injects a total energy of 10^{51} erg into the ISM.

The radio measurements are based on the *JVLA* D-configuration observations presented in Wiegert et al. (2015). The edge-on orientation of the CHANG-ES galaxies highlights the multiwavelength emission from the galactic haloes. Compared to previous observations, our *JVLA* observations are deep enough to detect the extended halo component and have high enough resolution to detect and remove bright point-like sources. Therefore, with the high-sensitivity, broad-band *JVLA* data we are not only able to use the most accurate radio continuum measurements of a complete flux-limited nearby edge-on spiral galaxy sample, but are also able to study the spatial variation of the radio continuum properties in both disc and halo of individual galaxies. Some preliminary results of these spatially resolved studies are presented in Wiegert et al. (2015) and will be further discussed in companion CHANG-ES papers. We have removed all the disconnected point-like sources around the galaxies but have included the AGN and any extended extraplanar features in the final radio flux measurement. Therefore, the radio luminosities quoted in this paper are the emission from the whole galaxy, including the contributions from both the disc and the halo. We adopt bandwidths of 2 GHz and 500 MHz in C and L bands in order to convert the radio flux density to luminosity ($L_{6\,GHz}$ and $L_{1.6\,GHz}$) for the convenience of comparison to L_X and $\dot{E}_{SN}$. We also calculate the integrated spectral index between C and L bands, which is defined as $S(\nu) \propto \nu^{-\alpha}$, where $S(\nu)$ is the global flux density in C and L bands, respectively. $L_{6\,GHz}$, $L_{1.6\,GHz}$, and α are also listed in Table 1.

There is an amount of missing flux density that mainly depends on the spatial scale of the emission features and the array

configuration. For D-configuration in *L* band, the largest angular scale is ∼16.2 arcmin, larger than the optical diameter (D_{25}) of all the CHANG-ES galaxies (Irwin et al. 2012a). In most of the cases, even some starburst galaxies, the vertical extension of the radio continuum emission is no larger than the extension in the radial direction (e.g. Irwin et al. 2013b). Therefore, the *L*-band data should include all the emission from the galaxy. For D-configuration in *C* band, however, the largest angular scale is ∼4 arcmin, smaller than the optical diameter of most of the CHANG-ES galaxies. We are thus likely resolving out some extended diffuse emission. Comparison with the catalogue of Gregory & Condon (1991) suggests that we are typically missing ≲50 per cent of the diffuse flux density in the more extended CHANG-ES galaxies (assuming a spectral index of $\alpha \sim 1.0$ and ignoring the AGN). To accurately measure the amount of missing flux density, deep single-dish observations are required. In general, larger galaxies and/or intense star-forming galaxies may have large-scale radio continuum features, so a larger fraction of missing flux density in *C* band.

16 of the CHANG-ES galaxies are included in the *Chandra* sample of nearby edge-on disc galaxies (Li & Wang 2013a,b; Li et al. 2014, Table 1); their soft X-ray luminosities are quoted from Li & Wang (2013a). *Chandra* data calibration and analysis are presented in Li & Wang (2013a) and statistical analysis of the X-ray properties of the galaxies are presented in Li & Wang (2013b) and Wang et al. (2015). We further compare the X-ray measurements to cosmological hydrodynamical simulations of hot galactic coronae in Li et al. (2014). In particular, the edge-on galaxies often show clear absorption features at the location of the galactic disc (Li & Wang 2013a). In order to have a uniform comparison among different galaxies, we first fit the extraplanar diffuse X-ray profile with an exponential model after removing the point-like sources and the regions heavily affected by disc absorption. The X-ray luminosities are measured within a vertical distance of five times the exponential scaleheight, after quantitatively removing the contributions from unresolved stellar sources and correcting for the filtered absorbing galactic disc by interpolating the diffuse X-ray intensity profile (Li & Wang 2013a). The X-ray luminosities are scaled to the distances of the CHANG-ES galaxies adopted in this paper.

2.2 Subsample definition

The presence of radio-bright (RB) AGN and sometimes even extended features related to the AGN could significantly affect the radio flux density measurements of the galaxies. The identification and properties of the AGN of the CHANG-ES galaxies will be presented in detail in a separate paper. In this paper, we identify 13 galaxies with RB AGN, satisfying at least one of the following criteria. (1) The galaxy has an unresolved radio core in higher resolution (B- or C-configuration) radio images which also shows polarization features and/or negative radio spectral index α; (2) There are lines of evidence for the existence of an outflow (e.g. radio jets or bubbles); (3) By comparing with archival radio data, there is significant radio flux variability of the core of the galaxy; (4) The galaxy has abnormal IR colour in *WISE* bands in the nuclear region; (5) An AGN is identified in the literature (see a summary of the archival identification of AGN for the CHANG-ES galaxies in Irwin et al. 2012a).

All the galaxies identified as hosting a RB AGN satisfy criterion (1). We further define a galaxy with an extremely radio bright ('ERB') AGN only if at least one of the additional criteria (2) or (3) is satisfied. These eight 'ERB' galaxies are: NGC 660 (jet, variability; Argo et al. 2015), NGC 2992 (extended nuclear radio

structure; Gallimore et al. 2006), NGC 3079 (radio lobe; Gallimore et al. 2006), NGC 4388 (jet; Hummel & Saikia 1991), NGC 4438 (jet, Hummel & Saikia 1991; to be presented in a separate CHANG-ES paper, Damas et al., in preparation), NGC 4594 (jet, Hada et al. 2013; variability, Krause, Wielebinski & Dumke 2006), NGC 4845 (variability, Irwin et al. 2015), and NGC 5084 (extended nuclear radio structure; the results will be presented in a separate CHANG-ES paper). We identify five other galaxies with 'RB' AGN (Table 1). Although some of the galaxies labelled with 'ERB' are indeed classified as radio quiet in the literature (e.g. Gallimore et al. 2006), in the CHANG-ES sample their radio flux densities are in general significantly affected by the presence of the AGN. In the following sections, we will compare the results of statistical analysis with and without these 'ERB' galaxies included in the sample, while 'RB' galaxies are still treated as normal galaxies with radio faint nuclei in all the calculations. All the 'ERB' and 'RB' galaxies will be plotted with different symbols in the figures presented in this paper.

We also include the Milky Way (MW) in some of our plots for comparison. The *L*-band radio luminosity is obtained from Strong et al. (2010) and converted to the same frequency and bandwidth as the CHANG-ES sample, assuming a spectral index of $\alpha \sim 0.8$. The error is calculated from the standard deviation of the luminosities of different models discussed in Strong et al. (2010). The final *L*-band luminosity of the MW adopted in this paper is $L_{1.6GHz,MW} = (6.1 \pm 2.0) \times 10^{36}$ erg s^{-1}. The SFR of the MW is taken to be $\mathrm{SFR}_{MW} = (1.065 \pm 0.385)$ M$_\odot$ yr^{-1} (Robitaille & Whitney 2010). The stellar mass of the MW is taken to be $M_{*,MW} = (6.43 \pm 0.63) \times 10^{10}$ M$_\odot$ (McMillan 2011). The soft X-ray luminosity of the MW is estimated from the *ROSAT* All Sky Survey: $L_{X,MW} \sim 2 \times 10^{39}$ erg s^{-1} (Snowden et al. 1997).

Similar to Li & Wang (2013a), we also define some subsamples for the convenience of comparison among different types of galaxies. Different subsamples described below will be plotted as different symbols in the following statistical analysis.

We use the local galaxy number density (ρ; Irwin et al. 2012a) to characterize the galaxy environment, and define galaxies with $\rho \leq 0.6$ as being in the field, while those with $\rho > 0.6$ as being clustered. This is just a general classification to characterize the global environment of the galaxies. We caution that some galaxies in poor groups or interacting galaxies with close companions (e.g. NGC 3432; English & Irwin 1997) have been classified as in the field, because they are not in rich clusters with a dense intracluster medium (ICM).

We also separate early- and late-type disc galaxies with their morphological type code (TC, Table 1). Galaxies with TC ≤ 1.5 are Sa or S0 and are defined as early-type, while others are late-type. This is again a general classification without considering the highly distorted morphology of some interacting galaxies (e.g. NGC 660).

The star formation properties adopted in this paper are estimated based on spatially resolved mid-IR images (Wiegert et al. 2015), which allow us to estimate the SFR surface density, rather than just the global integrated IR luminosities adopted in Li & Wang (2013a). We therefore adopt a new criterion to define starburst and non-starburst galaxies, i.e. those with both SFR ≥ 1 M$_\odot$ yr^{-1} and SFR surface density ≥ 2×10^{-3} M$_\odot$ yr^{-1} kpc^{-2} are starbursts while others are non-starbursts (Fig. 1a). Such a definition of a starburst galaxy is roughly consistent with the criteria adopted in Li & Wang (2013a) based on IR luminosity and colour. It is expected from both theoretical and observational studies that only starburst galaxies with a SFR surface density above a threshold should have a significant amount of extraplanar hot gas blown out of the disc

(Strickland et al. 2004; Li & Wang 2013b). NGC 4438 and NGC 5084 have extremely high SFR surface density (Fig. 1a). In these two galaxies, most of the *WISE* IR flux comes from the nucleus, but it is uncertain how much of it is due to star formation or an AGN.

3 STATISTICAL ANALYSIS

Similar to Li & Wang (2013b), we also utilize the Spearman's rank order correlation coefficient (r_s; by definition, $|r_s| < 1$, negative means anticorrelation) to describe the tightness of a correlation. We consider $|r_s| \geq 0.6$ as a tight correlation, $0.3 \leq |r_s| < 0.6$ as a weak correlation, and $|r_s| < 0.3$ as no correlation. We further characterize some important relations with simple expressions, with the corresponding root mean square (rms) around the best-fitting relations describing the dispersion. In order to fit a relation and to estimate the uncertainties of r_s and rms, we first generate 1000 bootstrap-with-replacement samples of the primary data and then resample each data point, assuming a normal distribution. For each re-generated sample, we fit the data with the same model and measure the model parameters, as well as r_s and rms, in the same way. These measurements are then rank ordered; their 68 per cent percentiles around the original fitting parameters, r_s and rms, are finally used as the estimates of their $1 - \sigma$ errors presented in figures and equations. Whenever we need to fit the logarithmic slope of a relation, we perform a linear fit with the IDL function '*ladfit*' in a logarithmic scale for both *x* and *y* axes. The '*ladfit*' function uses a robust least absolute deviation method and has the advantage of being less affected by some significantly outlying data points. In the following sections, the eight galaxies whose radio fluxes are highly affected by the AGN ('ERB' in Table 1) will not be included in quantitative calculations of r_s and rms presented in the figures, but we will compare the fitted relations between different galaxy parameters including these 'ERB' galaxies or not.

3.1 Statistical analysis of the diffuse radio continuum emission

In Fig. 2, we plot the radio continuum luminosities in *C* and *L* bands against various galaxy properties (SFR, M_*, M_{TF}). The MW is also included in Figs 2(b,d) for comparison, but it is not included in any quantitative calculations, such as the fitting of the relations and the calculation of r_s and rms. Galaxies with ERB AGN (symbols surrounded with a thick blue circle in the figures and listed as 'ERB' in the last column of Table 1) are also excluded from these quantitative calculations. In general, there are tight, weak, and no correlations between the radio luminosities and the SFR, M_*, and M_{TF}, respectively. The MW is consistent with other galaxies, but may be slightly less luminous in *L* band. Most of the 'ERB' galaxies are significant outliers in Figs 2(a,b), with unusually high radio continuum luminosities.

The L_{radio}–SFR correlations shown in Figs 2(a,b) are so tight that we can determine the logarithmic slopes of the relations. As the SFR adopted here is linearly related to the IR luminosity (L_{IR}; Jarrett et al. 2013), the slopes of the L_{radio}–SFR relations (L_{radio} represents the *C*- and *L*-band luminosities $L_{6\,GHz}$ and $L_{1.6\,GHz}$) are also representative of the slopes of the L_{radio}–L_{IR} relations which have been extensively studied in the literature (e.g. Helou et al. 1985; Yun et al. 2001; Bell 2003; Vlahakis et al. 2007; Basu et al. 2015b). The best-fitting L_{radio}–SFR relations are consistent with a linear slope within 1σ for *C* band and a significantly superlinear slope at ∼2σ confidence

level for *L* band (errors are quoted at 1σ confidence level):

$$L_{6\,GHz}/10^{38} \text{erg s}^{-1} = (0.233 \pm 0.022)$$
$$\times (\text{SFR}/\text{M}_\odot \text{ yr}^{-1})^{1.057 \pm 0.075} \quad (1)$$

and

$$L_{1.6\,GHz}/10^{38} \text{erg s}^{-1} = (0.188 \pm 0.012)$$
$$\times (\text{SFR}/\text{M}_\odot \text{ yr}^{-1})^{1.132 \pm 0.067}. \quad (2)$$

The tight correlations between L_{radio} and SFR indicate that young stars should be the major energy source of the radio continuum emission in most of the galaxies, regardless of its thermal or non-thermal origin. In addition, the weak and largely scattered L_{radio}–M_* correlations (also consistent with a linear slope) indicate that old stars traced by near-IR (*K*-band) emission could also contribute.

The tight correlation between v_{rot} and M_* (Fig. 1b) indicates that M_{TF} should be a good tracer of the mass of the galaxies. However, there is no correlation between L_{radio} and M_{TF}, which apparently indicates that the tight L_{radio}–SFR and possibly the weak L_{radio}–M_* correlations are not only a scaling effect in the sense that larger galaxies have more of everything. Although in most of the cases the distribution of individual galaxies are quite similar on the L_{radio}–M_* and L_{radio}–M_{TF} relations, the L_{radio}–M_{TF} relation indeed has much weaker correlation. No matter we include or remove the most significant outlier NGC 2992, which has a clearly warped disc potentially affecting the v_{rot} measurement, the correlation coefficient r_s of the L_{radio}–M_{TF} relation is close to 0.

There are several possible reasons which could enlarge the scatter of the L_{radio}–M_{TF} relation. *First*, the inclination correction for v_{rot}, which is a key to calculate M_{TF}, is based on the optical inclination angle *i*. *i* is for the stellar component (morphologically determined) and is not necessarily the same as the inclination angle of the gas component (often kinematically determined). Such a difference could add scatter to the derived M_{TF}. *Secondly*, M_{TF} is being derived from a mean relation (the baryonic Tully–Fisher relation with the stellar mass measured from the *K*-band luminosity; Fig. 1b) with a typical scatter of $\gtrsim 0.1$ dex (Bell & de Jong 2001), which could add some scatter to the L_{radio}–M_{TF} relations. *Thirdly*, M_{TF} includes the contribution from the H I gas, which could contribute to the total gravity (in fact, M_{TF} is derived from v_{rot} which is a direct tracer of the total gravity) but is not directly related to the SNe energy injection. The lack of correlation between L_{radio} and M_{TF} thus indicates that the weak L_{radio}–M_* correlations are really produced by processes related to stellar feedback, instead of a purely gravitational effect as is often important in the X-ray emitting hot haloes (Li & Wang 2013b; Li et al. 2014). *Fourthly*, the rotation velocity of some galaxies are significantly affected by tidal interaction (e.g. NGC 2992; Fig. 1b). M_{TF} of these galaxies does not trace their mass.

Both young and old stellar populations contribute to the generation of the radio continuum emission. Similar to Li & Wang (2013b), we also combine the contributions of young and old stellar populations to the energy budget by defining a total SN energy injection rate of $\dot{E}_{SN(Ia+CC)} = \dot{E}_{SN,Ia} + \dot{E}_{SN,CC}$. In some of the galaxies, especially early-type ones, Type Ia SNe contribute (apparently) $\gtrsim 80$ per cent of $\dot{E}_{SN(Ia+CC)}$ (Table 1). These galaxies are quiescent in star formation, and Type Ia SNe should dominate the overall activity of all ISM/CGM phases (e.g. NGC 4594; Li Z. et al. 2011).

The best-fitting L_{radio}–$\dot{E}_{SN(Ia+CC)}$ relations are

$$L_{6\,GHz}/10^{38} \text{erg s}^{-1} = (0.067 \pm 0.015)$$
$$\times (\dot{E}_{SN(Ia+CC)}/10^{41} \text{erg s}^{-1})^{1.100 \pm 0.123} \quad (3)$$
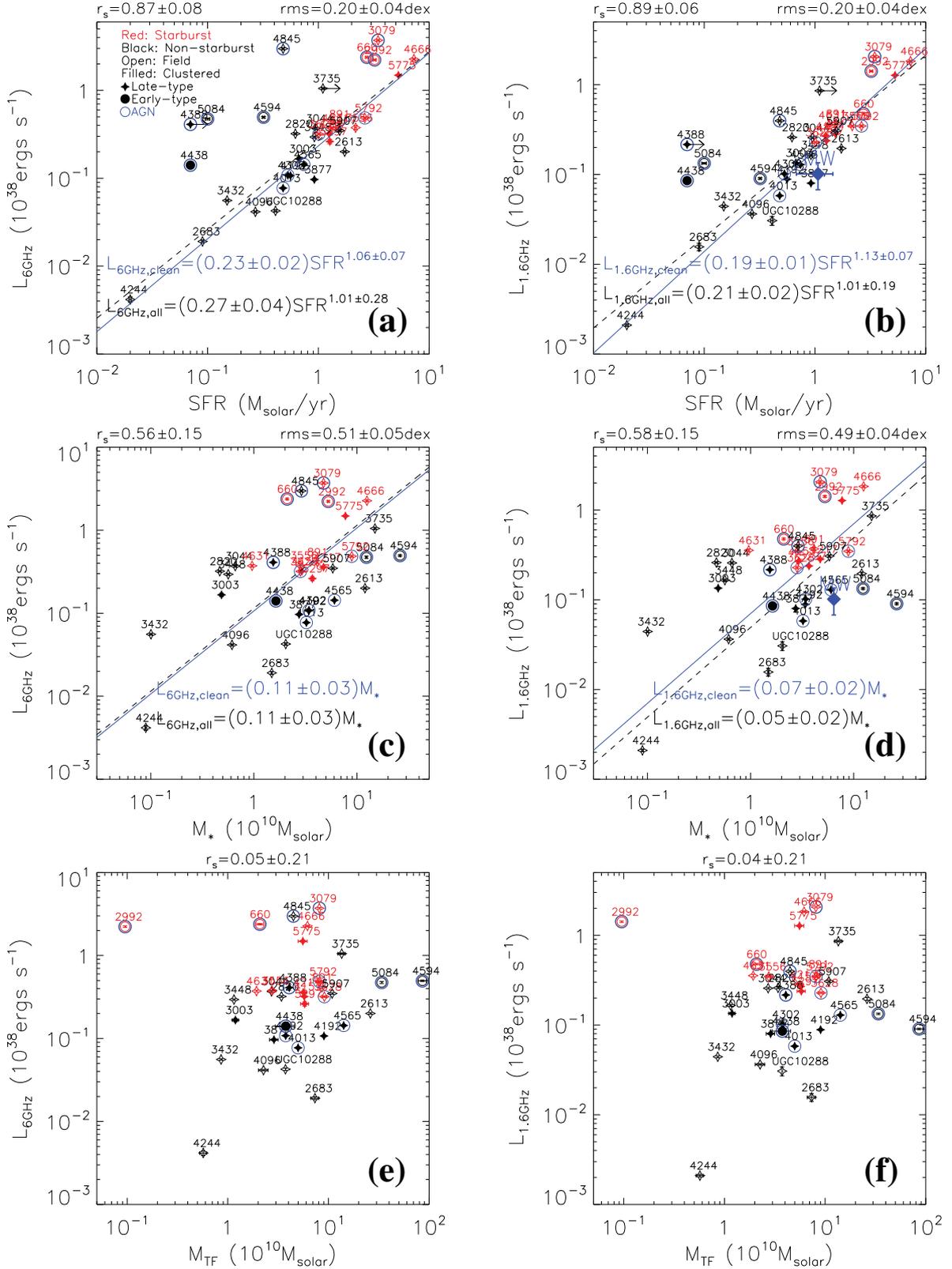
Figure 2. The *C*-band (6 GHz) and *L*-band (1.6 GHz) radio continuum luminosities plotted against the SFR, M_*, and M_{TF} of the CHANG-ES galaxies. Different subsamples are plotted with different symbols, as denoted in the upper-left corner of panel (a). The blue diamond in panels (b) and (d) denotes the MW. Names of the galaxies are denoted beside the data points. We show above each panel the Spearman's rank order correlation coefficient (r_s) of each relation for galaxies whose radio fluxes are not highly affected by the presence of a RB AGN. We further fit the L_{radio}–SFR and L_{radio}-M_* relations for these galaxies alone (the blue solid lines in panels a–d) and present the best-fitting relations as well as the $1 - \sigma$ errors of the model parameters on the figures. The rms of the data points around the best-fitting relations are presented at the top right of each panel. For comparison, we also fit the relations for the whole sample including the highly AGN-contaminated galaxies, present the best-fitting relations in black, and plot them as black dashed lines.

and

$$L_{1.6\,\mathrm{GHz}}/10^{38}\mathrm{erg\ s}^{-1} = (0.053 \pm 0.008)$$
$$\times (\dot{E}_{\mathrm{SN(Ia+CC)}}/10^{41}\mathrm{erg\ s}^{-1})^{1.175\pm0.102}, \quad (4)$$

which also have slightly superlinear slopes at least for *L* band ($\sim 2\sigma$ level). We do not find a significant improvement of the correlation by including the contribution from Type Ia SNe (as compared to the correlation with the SFR). Such an improvement of the correlation of X-ray emission with $\dot{E}_{\mathrm{SN(Ia+CC)}}$ is seen by Li & Wang (2013b), possibly because there are more early-type galaxies in Li & Wang (2013b)'s sample.

We further study the integrated radio spectral index between *C* and *L* bands (α; Table 1), which is quite indicative of the origin of the radio continuum emission. In general, we do not find a clear trend in any relations between α and other galaxy properties. The positive correlation between α and the SFR is only marginal ($r_{\mathrm{s}} = 0.30 \pm 0.18$; Fig. 4a). α typically spans a range of ~ 0.5–1.1, except for several significant outliers which will be further discussed in Section 3.2. The relatively low scatter of α is also indicated by the extremely tight *linear* correlation between the *C*-band and *L*-band luminosities (Fig. 4b), which also indicates that the emission in these two bands are produced by closely related processes.

There is a linear correlation between the point-source-removed truly diffuse halo soft X-ray luminosity and the IR luminosity of *spiral* galaxies (e.g. Strickland et al. 2004; Tüllmann et al. 2006; Li & Wang 2013b). This correlation is even preserved on subgalactic scale (e.g. Li et al. 2008). Li & Wang (2013b) further find a significantly improved tight linear correlation between the halo X-ray luminosity and the total (CC+Ia) SN energy injection rate of the galaxy. This correlation indicates a roughly constant and extremely low efficiency $\sim (0.4 \pm 0.1)$ per cent of converting the SN energy into the halo X-ray emission. The L_{radio}–$\dot{E}_{\mathrm{SN(Ia+CC)}}$ relations (Fig. 2, equations 3 and 4) have even tighter correlation and less scatter but the slopes are likely steeper than the L_{X}–$\dot{E}_{\mathrm{SN(Ia+CC)}}$ relation (assumed to be linear in Li & Wang 2013b). The different L_{radio}–$\dot{E}_{\mathrm{SN(Ia+CC)}}$ and L_{X}–$\dot{E}_{\mathrm{SN(Ia+CC)}}$ relations indicate non-linear L_{radio}–L_{X} relations and higher $L_{\mathrm{radio}}/L_{\mathrm{X}}$ ratio at higher SFR. These trends are revealed in Fig. 5, in panels (b) and (d) in which the MW is also consistent with other galaxies.

The best-fitting $L_{6\,\mathrm{GHz}}$–L_{X} and $L_{1.6\,\mathrm{GHz}}$–L_{X} relations are

$$L_{\mathrm{X}}/10^{38}\mathrm{erg\ s}^{-1} = (76.5 \pm 20.9)$$
$$\times (L_{6\,\mathrm{GHz}}/10^{38}\mathrm{erg\ s}^{-1})^{0.79\pm0.17} \quad (5)$$

and

$$L_{\mathrm{X}}/10^{38}\mathrm{erg\ s}^{-1} = (80.8 \pm 26.3)$$
$$\times (L_{1.6\,\mathrm{GHz}}/10^{38}\mathrm{erg\ s}^{-1})^{0.72\pm0.19}, \quad (6)$$

with sublinear slopes at $>1\sigma$ confidence levels. However, we caution that the best-fitting slopes of the L_{radio}–L_{X} relations are highly affected by the faintest galaxy NGC 4244. If we remove this galaxy, the best-fitting slopes will be consistent with linear or remain sublinear for non-AGN galaxies or the whole sample, respectively. The scatter will be larger, however, with the 1σ error of the slopes having typical values of ~ 0.3. There are also weak correlations between the $L_{\mathrm{radio}}/L_{\mathrm{X}}$ ratio and the SFR (Fig. 5c,d). All the relations shown in Fig. 5 indicate that higher SFR galaxies tend to convert a larger fraction of their SNe energy into non-thermal radio continuum emission than into thermal soft X-ray emission.

3.2 Significant outliers

In general, we do not find significant systematic differences between different pre-defined subsamples in the above statistical analysis. However, some galaxies show significantly different properties from others, indicating that their radio emission must have different origins. The nuclei of most of these galaxies are classified as 'ERB', apparently indicating that it is the AGN or the extended features related to the AGN which produce their unusual properties (e.g. NGC 4845; Irwin et al. 2015). In this section, we further discuss some additional peculiar properties of these outliers which may affect their multiwavelength appearance.

NGC 660 is unusually luminous in *C* band (Figs 2a, 3a) and faint in X-ray (Fig. 5), while its integrated radio spectral index is also extremely flat and even negative (Fig. 4a). The nucleus of this galaxy underwent a GHz-peaked outburst during our *JVLA* D-configuration observations (Argo et al. 2015), which will be further discussed in a separate paper. The *C* band in-band spectral index map of NGC 660 shows a well-resolved jet-like feature, which also has negative spectral index in the southeast half (Wiegert et al. 2015; note that the definition of α in this paper corresponds to $-\alpha$ in Wiegert et al. 2015). Therefore, it is most likely that the AGN and jet is responsible for the high luminosity in *C* band and the inverted radio spectral index in the integrated spectrum of this galaxy. NGC 660 is also the galaxy with the lowest X-ray radiation efficiency in Li & Wang (2013b)'s sample of 53 nearby edge-on galaxies (almost one order of magnitude lower than the best-fitting value). Such a low X-ray radiation efficiency is not yet fully understood, because the published X-ray observations of this galaxy by *Chandra* and *XMM–Newton* are rather poor and cannot detect the very extended component in the halo. NGC 660 is an interacting galaxy with a significant fraction of its cold gas widely distributed along the highly warped polar ring (Combes et al. 1992). This may help to explain its relative faintness in X-ray, which could be caused by the widely distributed star formation (possibly in the polar ring, which is *not* detected in X-ray; Li & Wang 2013a) and the low hot gas radiative cooling rate in the centre because of the lack of cool gas there.

NGC 4388 and NGC 4438 are unusually luminous in both *C* and *L* bands on the L_{radio}–SFR and L_{radio}–$\dot{E}_{\mathrm{SN(Ia+CC)}}$ relations (Figs 2a,b, 3). However, they are quite normal in radio spectral index (Fig. 4), and appear even brighter in X-ray (compared to radio; Fig. 5. NGC 4438 is also the galaxy with the highest X-ray radiation efficiency in Li & Wang 2013b's sample). These two galaxies are near the centre of the Virgo cluster and show significant tidal interactions with one of the most massive Virgo cluster members, M86 (Kenney et al. 2008). Their diffuse X-ray emission shows clearly distorted structures (Li & Wang 2013a). Furthermore, NGC 4438 is also found in our *JVLA* observations to have a single-sided radio lobe, and the radio lobe shows strikingly similar fine structure to the Hα and X-ray filaments (Machacek, Jones & Forman 2004; Kenney et al. 2008; Li & Wang 2013a). Therefore, in addition to the presence of the AGN, which is likely the major source of the enhanced radio emission, it is very likely that some environmental effects, such as ram-pressure stripping and/or compression, are affecting both the radio and X-ray properties of these two clustered galaxies (e.g. Murphy et al. 2009; Ehlert et al. 2013).

NGC 4594 and NGC 5084 are clearly more radio luminous than the best-fitting L_{radio}–SFR relations (Figs 2a,b; NGC 4594 is consistent with the best-fitting $L_{1.6\,\mathrm{GHz}}$–SFR relation), but are consistent with other galaxies on the L_{radio}–$\dot{E}_{\mathrm{SN(Ia+CC)}}$ relations (Fig. 3). They
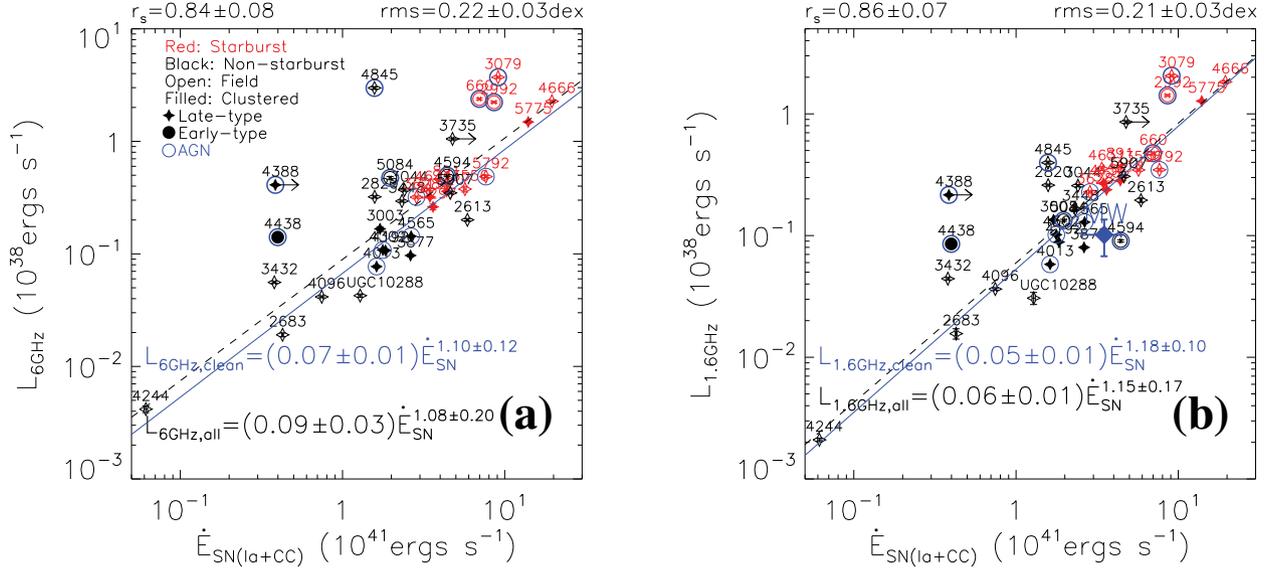
Figure 3. The *C*-band (6 GHz) and *L*-band (1.6 GHz) radio continuum luminosities plotted against the total (CC+Ia) SN energy injection rate ($\dot{E}_{\mathrm{SN(Ia+CC)}}$). Symbols are the same as shown in Fig. 2.
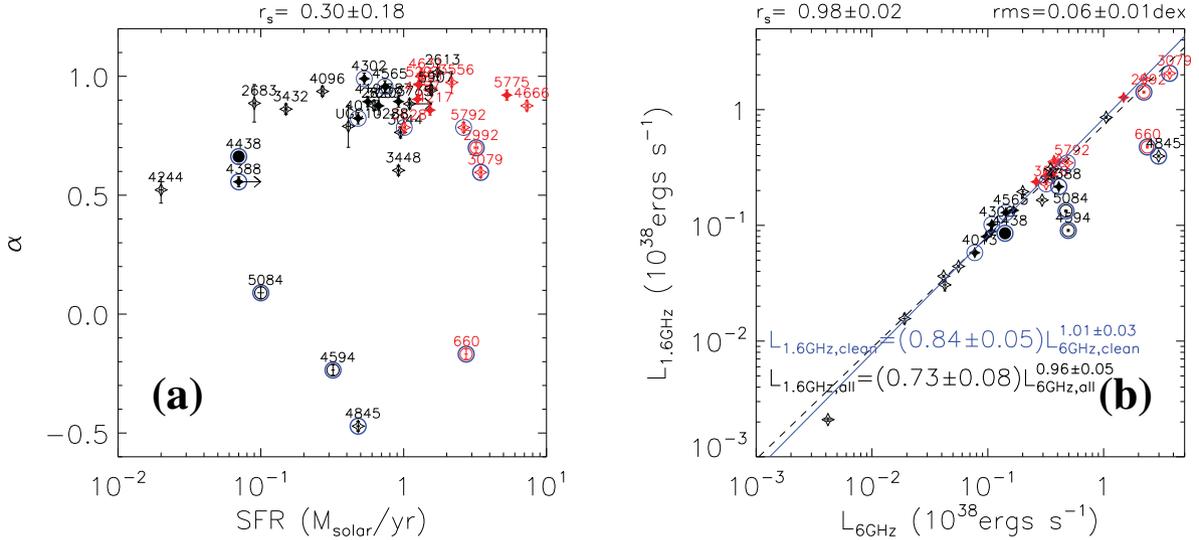

Figure 4. (a) The *C*-band (6 GHz) to *L*-band (1.6 GHz) spectral index (α) versus SFR. (b) Comparing the *C*-band and *L*-band luminosities of the galaxies. Symbols are the same as shown in Fig. 2.

both have flat radio spectra (Fig. 4), possibly caused by the presence of a low luminosity AGN (e.g. Hada et al. 2013). NGC 4594 and NGC 5084 are both very massive isolated early-type spiral galaxies. They also have the highest $\dot{E}_{\mathrm{SN,Ia}}/\dot{E}_{\mathrm{SN(Ia+CC)}}$ ratio among the sample galaxies ($\gtrsim 80$ per cent, Table 1). Therefore, it is very likely that a large fraction of the radio continuum emission is contributed by Type Ia SNe originating from old stellar populations (e.g. Li Z. et al. 2011).

4 DISCUSSION

Some results from in the above sections, such as the slopes of the L_{radio}–L_{IR} and the L_{X}–L_{radio} relations and the radio spectral index, are of great importance for understanding the origin, propagation, and energy loss of CR particles, as well as how SNe distribute their energy into different phases on galactic scales.

4.1 Compare the normalization of the radio–IR relationship to previous results

For the convenience of comparison with similar studies of the radio–IR relationship in the literature, we convert equations (1) and (2) to the form of

$$I_{6\,\mathrm{GHz}}/\mathrm{W\,Hz^{-1}} = (1.17 \pm 0.11) \times 10^{21}$$
$$\times (\mathrm{SFR/M_\odot\,yr^{-1}})^{1.057 \pm 0.075} \qquad (7)$$

and

$$I_{1.6\,\mathrm{GHz}}/\mathrm{W\,Hz^{-1}} = (3.76 \pm 0.24) \times 10^{21}$$
$$\times (\mathrm{SFR/M_\odot\,yr^{-1}})^{1.132 \pm 0.067}, \qquad (8)$$

where $I_{6\,\mathrm{GHz}}$ and $I_{1.6\,\mathrm{GHz}}$ are the spectral luminosities in units of W Hz^{-1}.
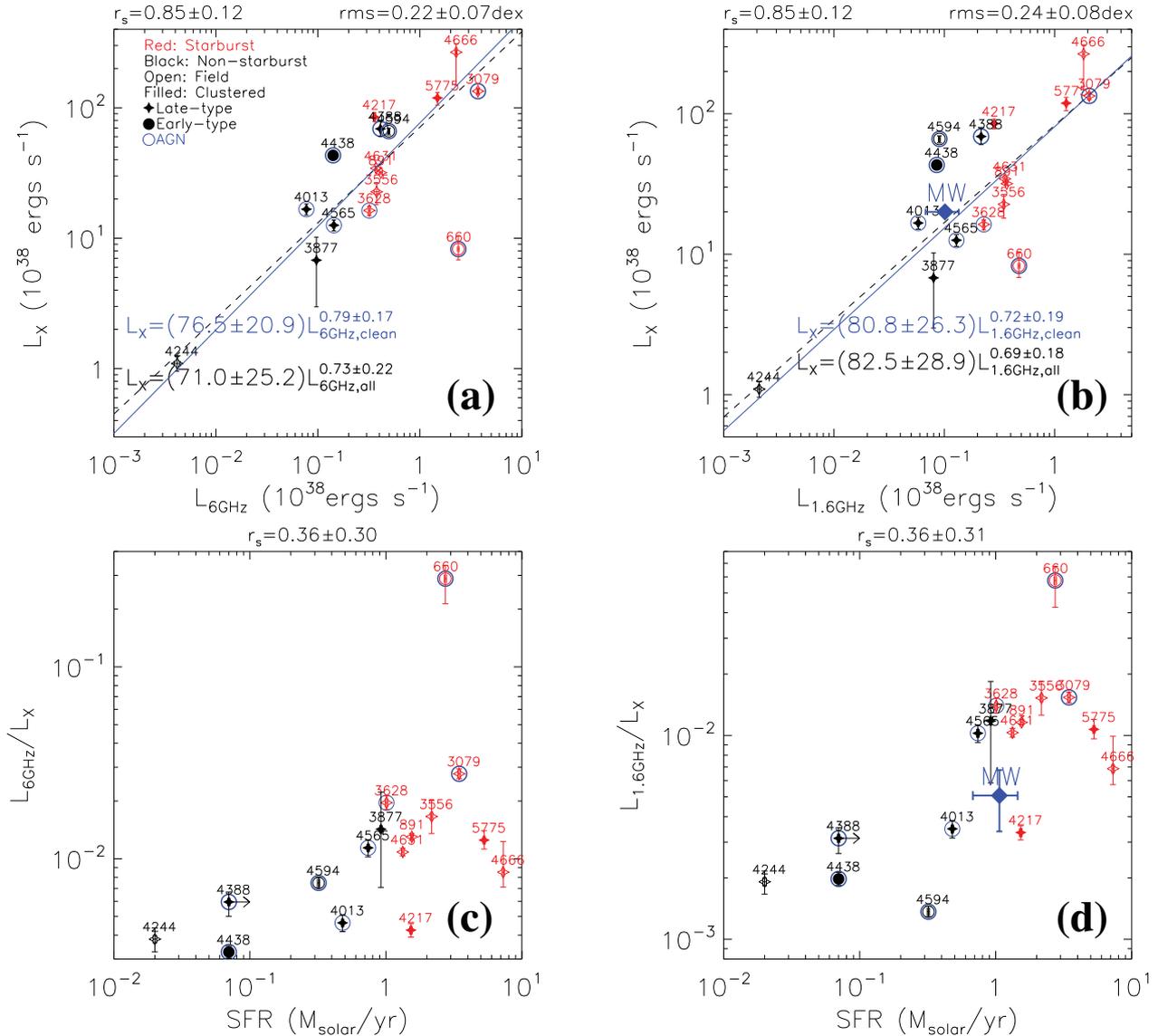
Figure 5. Comparison of the radio and X-ray emission of the CHANG-ES galaxies. X-ray luminosities are obtained from Li & Wang (2013a) and scaled to the distances adopted for the CHANG-ES galaxies in this paper. (a) L_X versus $L_{6\,GHz}$; (b) L_X versus $L_{1.6\,GHz}$; (c) $L_{6\,GHz}/L_X$ versus SFR; (d) $L_{1.6\,GHz}/L_X$ versus SFR. Symbols are the same as shown in Fig. 2.

The normalization of equation (8) is typically two to three times higher than those obtained in the literature based on spatially resolved observations of face-on galaxies. For example, Murphy et al. (2011) adopted a radio–SFR relation of $I_{1.4\,GHz}/W\,Hz^{-1} = 1.57 \times 10^{21}\,SFR/M_\odot\,yr^{-1}$ (converted from their equation 17), while Heesen et al. (2014) obtained a similar relation of $I_{1.4\,GHz}/W\,Hz^{-1} = 1.33 \times 10^{21}\,SFR/M_\odot\,yr^{-1}$ in their equation 1, which is a direct conversion from Condon, Cotton & Broderick (2002)'s relation by adopting a broken power-law initial mass function (IMF) from Calzetti et al. (2007). On the other hand, Yun et al. (2001) obtained an integrated (for the whole galaxy) radio–SFR relation of $I_{1.4\,GHz}/W\,Hz^{-1} = 1.69 \times 10^{21}\,SFR/M_\odot\,yr^{-1}$ in their large sample of 1809 galaxies. Considering the difference in IMF, their normalization should be 2.57×10^{21}, between our value and those from spatially resolved observations of face-on galaxies. The difference between $I_{1.4\,GHz}$ and the $I_{1.6\,GHz}$ in our equation (8) should be negligible. Therefore, compared to the papers on individual star forma-

tion regions in face-on galaxies, our integrated relation of edge-on galaxies has either overpredicted the radio flux or underpredicted the SFR.

We carefully checked our data calibration processes. In Paper IV and this paper, the SFR is estimated based on the *WISE* 22 μm luminosity using Jarrett et al. (2013)'s relation, which adopts the IMF described in Rieke et al. (2009, Section 2.1). There are 16 galaxies in the CHANG-ES sample overlapping with Li & Wang (2013a)'s sample, where they estimate the SFR from the *IRAS* total-IR luminosity using Kennicutt (1998)'s relation. The total-IR based SFR in Li & Wang (2013a) is on average ∼2.3 times of the mid-IR based SFR in this paper, after accounting for the different IMF adopted in these two papers, using the same definition of total-IR luminosity as Irwin et al. (2012a), and adopting the more recent *IRAS* fluxes (Sanders et al. 2003, while Li & Wang 2013a adopted the *IRAS* fluxes from Fullmer & Lonsdale 1989, which are compiled before the final calibration of the *IRAS* Level 1 Archive in May

1990). Our radio flux is in general consistent with those collected from the literature in Irwin et al. (2012a), except for several galaxies hosting an AGN in the outburst stage during the observations (e.g. NGC 4845; Irwin et al. 2015). Therefore, the discrepancy in the radio–IR relationships between our equation (8) and some papers could be attributed to several processes.

First, strong absorption by dust grains in the edge-on case may even affect the IR emission. The discrepancy between our radio–IR relation and that from Yun et al. (2001, which is also integrated for the whole galaxy) cannot be a result of the diffusion of CR electrons (with a typical length-scale of ∼kpc at *L* band, e.g. Berkhuijsen, Beck & Tabatabaei 2013). As already pointed out in Section 2.1, the average total-IR to mid-IR luminosity ratio of our sample is ∼18–60 per cent higher than those in Rieke et al. (2009) or Calzetti et al. (2010), which may be caused by the strong dust absorption in our edge-on galaxies. Although in many cases, the total-IR and mid-IR emission can be regarded as extinction free, this may not be true at high inclination angle of the galactic disc. The ∼2.3 times difference between the mid-IR and total-IR based SFR may explain the discrepancy in the radio–IR relation between our result and Yun et al. (2001)'s. However, we caution that Yun et al. (2001) adopted a far-IR based SFR which could be biased by the relatively strong contribution from cold dust heated by low-mass stars (see below). Furthermore, such a discrepancy in mid-IR and total-IR based SFRs also exists in other papers, e.g. ∼1.8 times for Rieke et al. (2009) and ∼1.4 times for Calzetti et al. (2010). A better estimate of the SFR should be based on an SED fit from radio to IR, especially by including the extinction free and thermal dominated 33 GHz emission (e.g. Murphy et al. 2011).

Secondly, heating of dust by non-ionizing photons from low-mass stars could contribute to the IR emission. Non-ionizing photons from low-mass stars could also contribute to the heating of the circumstellar dust so the IR emission (e.g. Temi et al. 2009). This IR emission is not related to the current star formation, so could bias the estimation of SFR based on any sort of dust-reprocessed IR emission. Murphy et al. (2011) found that the IR-based SFR in the nuclear region of NGC 6946 is clearly overestimated, probably because there are more old stars there. When estimating the SFR based on the *WISE* 22 μm luminosity, we have removed IR-bright AGN and only include the IR emission from the disc. This process may also reduce the contamination from old stars in the galactic bulge, thus results in a lower SFR.

4.2 The calorimeter condition and its effect on the radio–IR slope

We next roughly estimate the calorimeter conditions for CR leptons in galactic discs and haloes. The synchrotron cooling time-scale for CR electrons is $\tau_{\rm syn} \sim 10^9 \, {\rm yr} B^{-1.5} \nu^{-0.5}$, where B is the magnetic field strength measured in μG, and ν is the frequency of synchrotron emission measured in GHz (Beck & Wielebinski 2013). For a rough estimation, we assume the average magnetic field of a spiral galaxy is $B \sim 10$ μG. For *C* and *L* bands, the resultant $\tau_{\rm syn}$ are then ∼1.3 × 10^7 and ∼2.5 × 10^7 yr, respectively. For comparison, if we assume the CR electrons are entrained in a galactic wind with a typical velocity of ∼300 km s^{-1}, the typical escape time-scale will be ∼10^6 and 3 × 10^7 yr for a galactic disc with ∼300 pc scaleheight and a galactic halo with a typical size of ∼10 kpc, respectively. Therefore, a galactic disc is typically *not* a calorimeter for CR electrons entrained in galactic outflows. On the other hand, a galactic halo is closer to a CR electron calorimeter, with the real condition depending on the specific parameters. These estimates highlight the

importance of including the galactic halo (with a typical extension of ≲10 kpc for the CHANG-ES galaxies based on the D-configuration observations; Wiegert et al. 2015) into the energy budget of CRs, which could only be done with deep radio continuum observations such as those being carried out in the CHANG-ES programme.

Völk (1989) developed a calorimeter model in order to explain the tight radio–IR correlation. This model assumes that each galaxy act as a 'calorimeter' for both the relativistic electrons and the UV photons which heat the surrounding dust and are re-radiated in IR. The relativistic electrons lose energy mainly via synchrotron and inverse Compton (IC) processes. Therefore, in Völk (1989)'s model, the only factor that could modify the slope of the $L_{\rm radio}$–$L_{\rm IR}$ relation or the proportionality of the non-thermal radio emissivity to the SN rate is the average energy density ratio of the radiation and magnetic field $\bar{U}_{\rm rad}/\bar{U}_{\rm B}$ ($L_{\rm radio}/\dot{E}_{\rm SN} \propto (1 + \bar{U}_{\rm rad}/\bar{U}_{\rm B})^{-1}$). As the total (or random) magnetic field strength increases much slower than $\bar{U}_{\rm rad}$ with the SFR, and the ordered magnetic field even shows no clear increase (e.g. Stil et al. 2009; Krause 2011), the $\bar{U}_{\rm rad}/\bar{U}_{\rm B}$ ratio is expected to be higher for high-SFR galaxies (e.g. Thompson et al. 2006). Therefore, the calorimeter model predicts sublinear $L_{\rm radio}$–SFR or $L_{\rm radio}$–$\dot{E}_{\rm SN(Ia+CC)}$ relations, or less energy of CR electrons dissipated via synchrotron emission at higher SFR. The calorimeter model could successfully reproduce the global multiwavelength CR-related emission in the extended (e.g. ∼10 kpc) MW halo (Strong et al. 2010).

A non-calorimeter model discussed in Niklas & Beck (1997) predicts a logarithm radio–IR slope of ∼1.3. This model assumes equipartition between the energy densities of the CR and magnetic field, and adopts the *observed* dependencies of the SFR and the strength of the equipartition magnetic field on the density of the cool gas, as well as the slope of the radio synchrotron spectrum. In non-calorimeter models such as the Niklas & Beck (1997) model, it is natural to have non-calorimeter conditions on small scales or at low and moderate SFRs. In this case, most of the CR electrons escape from the galactic disc which accounts for a dominant fraction of the detected non-thermal radio emission. The production rate of CR electrons has a stronger dependence on the SFR ($\propto$ SFR) than the magnetic field energy density ($\propto B^2 \propto$ SFR$^{0.69}$; Niklas & Beck 1997). Therefore, although the synchrotron cooling time-scale decreases with increasing SFR (e.g. Lacki et al. 2010), it is still expected that the escape probability of CR electrons out of the galactic disc increase with the SFR (however, see an opposite trend predicted by Chi & Wolfendale 1990). However, unlike calorimeter models in which the non-thermal radio emission does not depend significantly on the magnetic field strength, the non-calorimeter energy equipartition model of Niklas & Beck (1997) predicts a strong dependence of the non-thermal radio emission on the magnetic field strength ($L_{\rm radio} \propto B^4 \propto$ SFR$^{1.37}$), which compensates the weak positive dependence of the escape probability on the SFR. In addition, it is not clear if the velocity of galactic wind depends significantly on the SFR or not. If so, the escaping time-scale should be shorter in high SFR galaxies, and the dependence of the escape probability on the SFR should be weaker. A combination of these effects naturally produces a superlinear radio–IR slope.

In conclusion, the radio–IR slope depends on the SFR. *At low and moderate SFR*, the magnetic field is low and the synchrotron radiative cooling time-scale is long, so most of the CR electrons could escape from the galactic disc. As predicted by Niklas & Beck (1997)'s non-calorimeter model, there is a superlinear radio–IR relation in this escape-dominated regime. On the other hand, *at high SFR*, the magnetic field (and also the radiation field) is high enough that most of the CR electrons lose their energy via
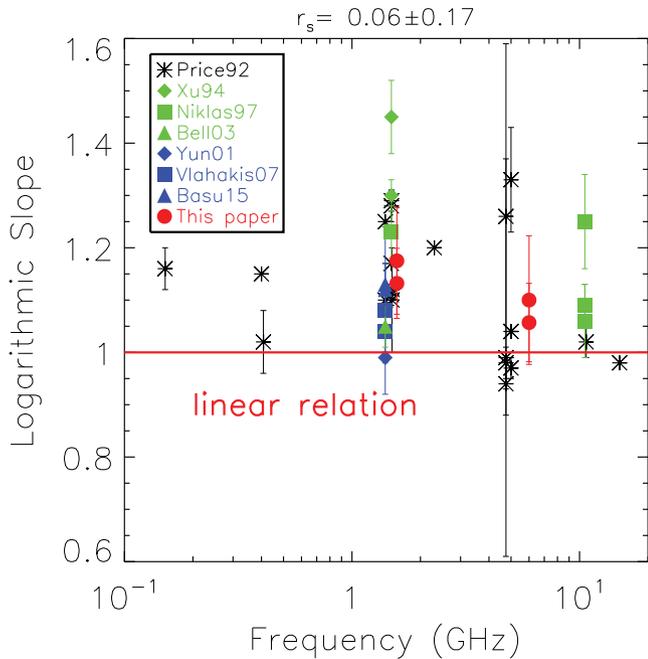
Figure 6. The logarithmic slopes of the L_{radio}–L_{IR} relations obtained from this paper (red filled circles; for both the L_{radio}–SFR and L_{radio}–$\dot{E}_{SN(Ia+CC)}$ relations of equations 1, 2, 3, and 4) and literature plotted against the centre frequency of the radio observations. The red solid line marks the slope of a linear relation. References of the data are denoted in the inset panel: Price92: early measurements collected by Price & Duric (1992), including their own measurements; Xu94: Xu et al. (1994); Niklas97: Niklas (1997); Yun01: Yun et al. (2001); Bell03: Bell (2003); Vlahakis07: Vlahakis et al. (2007); Basu15: Basu et al. (2015b).

synchrotron radiation or other cooling processes (e.g. IC) close to the disc. In this loss-dominated regime, a calorimeter condition is satisfied and the radio–IR relation is almost linear, or if the IC cooling is dominant, the relation can be even sublinear. We do *not* find significant evidence for the flattening of the radio–IR relation at high SFR within our sample. This is either because the SFRs of our sample galaxies are not as high as required by the loss-dominated regime, or because the escape time-scale also decreases with the SFR as a result of the possibly increasing wind velocity with the SFR (e.g. Krause 2009).

4.3 The observed slopes of the L_{radio}–SFR and L_{radio}–$\dot{E}_{SN(Ia+CC)}$ relations

In Fig. 6, we compare the logarithmic slopes of the L_{radio}–SFR and L_{radio}–$\dot{E}_{SN(Ia+CC)}$ relations (equations 1, 2, 3, and 4) to some archival measurements of the slopes of the L_{radio}–L_{IR} relations. We caution that these archival measurements are obtained with different samples, different radio observing depth and array configurations (or single-dish observations), different bands for IR luminosities, and sometimes even different redshifts. Therefore, the figure cannot be used for quantitative calculations.

Our measurements based on the CHANG-ES data show a clearly steeper slope in L band than in C band, and a significantly superlinear L_{radio}–L_{IR} relation in L band. However, the superlinearity in C band is quite marginal. The large scatter of the measurements obtained from different papers also prevents us from finding a clear trend of steeper L_{radio}–L_{IR} relations (larger slope) at lower frequencies as

claimed by Price & Duric (1992). Such a trend is expected if there is a lower fraction of non-thermal radio emission at high frequencies and/or a faster synchrotron energy loss and more calorimeter-like condition for higher energy CR electrons.

The discussions in Section 4.2 assume the radio continuum emission is mainly produced by the synchrotron process. However, the radio continuum emission at C and L bands actually include both thermal and non-thermal components (e.g. Price & Duric 1992; Dumke, Krause & Wielebinski 2000; Chyży et al. 2007; Krause 2009; Irwin et al. 2012b). The thermal radio emission is expected to be linearly dependent on the thermal IR emission produced by the dust-reprocessed high energy photons from young stars (e.g. Price & Duric 1992; Xu et al. 1994; Niklas 1997). As a result, in addition to a more calorimeter-like condition in C band, the flatter radio–IR relations in C band than in L band (Fig. 6) could also be partially caused by the larger contribution of thermal emission in C band.

Another possibility to explain the high L_{radio}/SFR or L_{radio}/$\dot{E}_{SN(Ia+CC)}$ ratios of high-SFR galaxies are the additional CR lepton sources in these galaxies. These additional CR leptons may come from the secondary electrons/positrons produced by the decay of charged pions (π^+ or π^-), which are produced in the interaction between CR hadrons and the ISM (e.g. Strong et al. 2007; Lacki et al. 2010). In a galaxy similar to the MW, typically $\sim$(10–20) per cent of the synchrotron energy loss in the radio band is caused by the secondary electrons/positrons (Strong et al. 2010). However, in intense star-forming galaxies, the ISM density is much higher, and the galaxy becomes a better calorimeter for CR protons due to frequent proton (CR)–proton (ISM) interaction and strong pion decay. In these galaxies, the secondary electrons could even dominate the primary ones (e.g. Domingo-Santamaría & Torres 2005; Lacki et al. 2010). Therefore, intense star-forming galaxies possibly have a higher non-thermal radio flux density per unit SFR or $\dot{E}_{SN(Ia+CC)}$ than inactively star-forming ones.

4.4 Radio spectral indices

The spatially integrated radio spectral index of the whole galaxy as presented in Fig. 4(a) could be influenced by various processes. In the absence of a RB AGN, there are three major components of the galactic radio continuum emission (Lisenfeld & Völk 2000): the thermal emission from HII regions, typically having a flat spectrum ($\alpha \sim 0.1$, e.g. Price & Duric 1992); the synchrotron emission from discrete SNRs with an almost constant spectral index of $\alpha \sim 0.5$ (Green 2014); and the diffuse synchrotron emission from the CR electrons spread over the entire galaxy, where the spectral index varies in a large range, typically from 0.5 to 1.1 (Lisenfeld & Völk 2000).

The integrated radio spectral index is quite indicative of the origin of the radio continuum emission. The steep spectrum or the large α ($\sim$0.5–1.1) of most of the sample galaxies is very consistent with a non-thermal origin of the radio continuum emission from the diffuse synchrotron component. However, the galactic scale diffuse synchrotron emission is affected by many factors (e.g. Strong, Orlando & Jaffe 2011; Orlando & Strong 2013; Basu et al. 2015a), such as the CR lepton spectral index integrated along the line of sight, the type of propagation (diffusion, convection, and re-acceleration processes), the relative importance of CR electron energy loss mechanisms (via synchrotron, IC, adiabatic loss, bremsstrahlung, and/or ionization), and the confinement of the CR electrons. The resultant spectral index of this component is thus highly variable, and its nature cannot be simply determined based on the spatially integrated spectral index alone.

On the other hand, a substantial, but not dominant contribution of thermal emission to the radio continuum is *not inconsistent* with the large measured α values. It is found that the relative contributions of the thermal and non-thermal components are always variable among galaxies (e.g. Chyży et al. 2007; Krause 2009), and a significant contribution from the thermal component has been revealed in several galaxies of our sample (e.g. NGC 5907; Dumke et al. 2000). Furthermore, the in-band spectral index maps of many CHANG-ES galaxies indicate clear spatial variations of α (Wiegert et al. 2015), with the radio spectrum often flattening towards the galactic disc, indicating a larger contribution from the thermal emission in the disc or a flattening of the synchrotron spectral index in star-forming regions (e.g. Tabatabaei et al. 2007; Basu & Roy 2013).

Fig. 4(a) shows only a very weak correlation between α and the SFR ($r_s = 0.30 \pm 0.18$ for all but 'ERB' galaxies). However, if we remove all the galaxies with AGN (both 'RB' and 'ERB'), the correlation becomes better ($r_s = 0.46 \pm 0.18$). The scatter in Fig. 4(a) is so large that we cannot accurately determine the α–SFR slope, but the weak correlation between α and the SFR is consistent with the difference between the slopes of the $L_{6\,GHz}$–SFR and $L_{1.6\,GHz}$–SFR relations. Even if we remove all the galaxies with AGN ('ERB'+'RB'), starburst galaxies on average still do not show significantly higher α than non-starburst ones, except for extremely quiescent galaxies such as NGC 4244. Therefore, although we cannot exclude a possible correlation between α and the SFR just based on the current data, it is clear that such a relation cannot be monotonic. There must be some mechanisms limiting the steepening of the radio spectrum at very high SFR.

Assuming the radio emission is dominated by the non-thermal component, it is expected that the calorimeter condition could strongly affect the radio spectral index (e.g. Lacki et al. 2010). For a very simple estimate under the assumption of continuous CR electron injection, by assuming an energy spectrum of CR electrons with a power-law index of $p \sim 2$–2.5, the radio synchrotron spectrum will have a spectral index of $\alpha \sim 1.0$–1.2 under calorimeter conditions. A flatter spectrum may indicate non-calorimeter conditions (e.g. Lacki et al. 2010). In high-SFR galaxies, the CR electron is often dominated by a single-injection population (e.g. Heesen et al. 2015). These starburst galaxies have strong magnetic fields, the rapid energy loss of CR electrons therefore produces a steep radio spectrum. This trend is in general consistent with a positive correlation between α and the SFR. However, on the other hand, extreme starburst galaxies often produce strong galactic winds or fountains which could enhance the escape of CR leptons via convection, therefore reducing the radiative loss and flattening the synchrotron spectrum. Furthermore, additional cooling of CR electrons in starburst galaxies, e.g. via ionization, could also flatten their radio spectra at low frequency (e.g. Thompson et al. 2006; Basu et al. 2015a). This suggests that extremely active or inactive star-forming galaxies tend to have flatter radio spectra, consistent with the trend shown in Fig. 4(a).

4.5 Regulation of SNe energy feedback in radio and X-ray bands

We first estimate the radiation efficiency of CR electrons in radio bands typically dominated by the non-thermal component (e.g. from 10 MHz to 10 GHz). As shown in equations (3) and (4), the SNe radiation efficiency in C and L bands (the fraction of SNe energy radiated in C and L bands) are $\eta_C \sim 8 \times 10^{-5}$ and $\eta_L \sim 5 \times 10^{-5}$, respectively. A direct power-law interpolation of η_C and η_L to the whole radio band dominated by non-

thermal emission results in an radio continuum radiation efficiency of $\eta_{radio} \equiv L_{10\,MHz-10\,GHz}/\dot{E}_{SN(Ia+CC)} \sim 8 \times 10^{-4}$. If we assume a SN could typically convert $\lesssim 10$ per cent of its mechanical energy into CRs (e.g. Kosenko, Ferrand & Decourchelle 2014), the estimated η_{radio} indicates ~ 1 per cent of the CR energy could be converted to radio continuum emission around the whole galaxy (including the halo). Since most of the radio continuum emission is produced by CR electrons, if we assume a calorimeter condition for the observed radio halo, this fraction of ~ 1 per cent is also the fraction of CR energy contained in electrons, and is consistent with the estimates for the MW (e.g. Strong et al. 2010). In conclusion, SNe could in general provide enough CR electrons responsible for the observed radio continuum emissions from the whole galaxy.

The X-ray properties of galaxies have much larger scatter than the radio properties. This is mainly because a galaxy is typically *not* a 'calorimeter' for X-ray emitting hot gas at least in the inner halo where most X-ray observations are sensitive enough (e.g. Li & Wang 2013a). On the other hand, a galactic halo is often a fairly good 'calorimeter' for radio continuum emitting CR electrons as discussed in Section 4.2. This difference results in a large scatter on the X-ray radiation efficiency η_X ($\equiv L_X/\dot{E}_{SN(Ia+CC)}$) and poorly constrained slopes of the X-ray related scaling relations (e.g. Fig. 5; Li & Wang 2013b; Wang et al. 2015), but a small scatter in η_{radio} and relatively tight L_{radio}–SFR and L_{radio}–$\dot{E}_{SN(Ia+CC)}$ relations (Figs 2a,b, 3). Therefore, our conclusions on the slopes of the scaling relations are mostly based on these tighter relations.

There are two possibilities to explain the trend of the dependence of the radio/soft X-ray luminosities on the SFR or $\dot{E}_{SN(Ia+CC)}$. *First*, as discussed in Sections 4.2 and 4.3, because of the strong dependence of the radio continuum emission on the magnetic field strength in non-calorimeter models and/or the larger contribution from secondary electrons, there is a higher radio radiation efficiency η_{radio} in higher SFR galaxies. *Alternatively*, the determination of the L_X–$\dot{E}_{SN(Ia+CC)}$ slope is less accurate (than the L_{radio}–$\dot{E}_{SN(Ia+CC)}$ or L_X–L_{radio} relations), for example, rms ~ 0.5 dex over ~ 3 dex of L_X or $\dot{E}_{SN(Ia+CC)}$ (Li & Wang 2013b). Therefore, it is also possible that the X-ray radiation efficiency η_X slightly decreases with increasing $\dot{E}_{SN(Ia+CC)}$. In fact, η_X spans a large range of ~ 2 dex, and depends on some other galaxy parameters, indicating that it could be affected by both cool–hot gas interaction and gravitational confinement (Li & Wang 2013b; Wang et al. 2015).

In the inner region of a galactic halo, the diffuse soft X-ray emission is often produced by a galactic superwind, fountain or subsonic outflow (e.g. Strickland et al. 2004; Li & Wang 2013b; Li et al. 2014). The galactic superwind could be launched by many mechanisms, such as the energy and momentum deposition by SNe, the radiation pressure, and/or the CRs (e.g. Everett et al. 2008; Hopkins, Quataert & Murray 2012). There are two key but poorly constrained parameters which could determine how strong the X-ray emission related to this superwind is: the thermalization efficiency of the SNe energy and the mass loading efficiency into the wind (e.g. Chevalier & Clegg 1985; Strickland & Stevens 2000; Strickland & Heckman 2009; Wang et al. 2015). Zhang et al. (2014) show that if the thermalization efficiency and the mass loading efficiency are both constant, the X-ray luminosity of a galactic wind should be $\propto \text{SFR}^2$, much steeper than the observed linear relations (e.g. Li & Wang 2013b). Instead, either or both efficiencies must vary with the SFR. Zhang et al. (2014) further show that the mass loading efficiency could decrease significantly in high-SFR galaxies. This result is consistent with the observed anticorrelation between the X-ray radiation efficiency η_X and the CC SN rate surface density (Li & Wang 2013b; Wang et al. 2015), as well as the trend between

the X-ray brightness of a sample of earlier-type galaxies and the cool gas content (Li et al. 2011). In conclusion, the X-ray radiation efficiency could decrease with increasing SFR, but this is most likely an effect of the decreasing mass loading efficiency, and we do *not* have direct evidence that a galaxy distributes a smaller fraction of its SNe feedback energy into galactic superwinds.

5 SUMMARY AND CONCLUSIONS

It is widely believed that SNe and SNRs are the major sources of CR leptons, which lose their energy via synchrotron radiation and other processes, producing the radio continuum emission in galaxies. The extended radio continuum halo detected in some nearby galaxies strongly suggests that galaxy discs are *not* calorimeters for CR electrons. However, whether or not a galactic *halo* satisfies the calorimeter condition is still under debate and could be affected by many factors.

Thanks to the high sensitivity and angular resolution of the *JVLA*, we obtain reliable spatially resolved measurements of the *diffuse* radio continuum properties of a flux-limited nearby edge-on spiral galaxy sample (CHANG-ES; Irwin et al. 2012a; Wiegert et al. 2015). The CHANG-ES data enable us, for the first time, to include the galactic radio halo into the energy budget for a statistically meaningful sample. In this paper, we perform statistical analyses, comparing the integrated diffuse radio continuum luminosity of the whole galaxy (including both disc and halo) to other galaxy properties. The MW is also included for comparison. Our main results and their scientific implications are summarized below.

(1) We compare the *C*- and *L*-band radio continuum luminosities to the SFR (estimated from the spatially resolved *WISE* mid-IR photometry), stellar mass (M_*, estimated from the *2MASS* near-IR photometry), and total baryonic mass (M_{TF}, estimated from the gas rotation velocity) of the galaxies. We find tight L_{radio}–SFR and weak L_{radio}–M_* correlations, indicating that young stars are the major energy sources of, while old stars could also contribute to, the radio continuum emission. The lack of L_{radio}–M_{TF} correlation further indicates that the L_{radio}–SFR and L_{radio}–M_* correlations are not only a scaling effect in the sense that larger galaxies have more of everything. The MW is in general consistent with the best-fitting relations of other galaxies within the scatter.

(2) We combine the contributions from the energy injection of CC and Type Ia SNe ($\dot{E}_{SN(Ia+CC)}$), which are proportional to the SFR and M_*, respectively. The tight and low-scatter L_{radio}–$\dot{E}_{SN(Ia+CC)}$ correlations indicate that the radio continuum emission on average accounts for $\sim 8 \times 10^{-4}$ of the total SNe energy injection rate. This radio radiation efficiency is consistent with the expected energy contained in CR electrons, which suggests that the observed radio halo of the CHANG-ES galaxies are very close to a calorimeter of the CR electrons.

(3) The scatter of the L_{radio}–SFR and L_{radio}–$\dot{E}_{SN(Ia+CC)}$ relations are so small (rms $\lesssim 10$ per cent of the logarithmic covering range of the parameters) that we could accurately constrain their logarithmic slopes, which are clearly (at $\sim 2\sigma$ confidence level) superlinear in *L* band (1.132 ± 0.067 and 1.175 ± 0.102 for the L_{radio}–SFR and L_{radio}–$\dot{E}_{SN(Ia+CC)}$ relations, respectively) while marginally (within $\sim 1\sigma$) consistent with linear in *C* band (1.057 ± 0.075 and 1.100 ± 0.123 for the L_{radio}–SFR and L_{radio}–$\dot{E}_{SN(Ia+CC)}$ relations, respectively).

(4) The normalization of our $I_{1.6\,GHz}/W\,Hz^{-1}$–SFR relation is typically two to three times higher than those obtained in some papers based on spatially resolved observations of face-on galaxies, indicating that we have either overpredicted the radio flux or under-

predicted the SFR compared to these works. This discrepancy may plausibly be explained by the enhanced extinction in our edge-on galaxies even in IR, while it could also be affected by the heating of the dust by non-ionizing photons from low-mass stars in the galactic bulge.

(5) The integrated radio spectral index between *C* and *L* bands is large ($\alpha \sim 0.5$–1.1) for most of the sample galaxies, apparently consistent with a non-thermal origin from the galaxy-wide diffuse synchrotron emission in both bands. However, we cannot rule out a considerable contribution from the thermal emission, which may add scatter to the measured α and also contribute to the spatial variation of the in-band spectral index maps as presented in Wiegert et al. (2015).

(6) Based on the halo diffuse soft X-ray luminosity L_X measured with the *Chandra*, we find sublinear L_X–L_{radio} slopes in both *C* and *L* bands. Furthermore, the L_{radio}/L_X ratio also weakly depends on the SFR. Therefore, there is a faster increase of radio continuum emission than X-ray emission with increasing SFR.

(7) There are several galaxies with RB AGN that they show clearly different radio and/or X-ray properties from other galaxies. They are typically more radio luminous and have flat radio spectra. In addition to the contamination from the AGN, some of these outliers also exhibit peculiar properties, such as tidal interactions, environmental effects related to the ICM, and large contributions from the feedback of Type Ia SNe. These unusual properties may further affect their radio and X-ray properties.

Although the overall energy budget indicates that the galactic radio continuum halo detected by the CHANG-ES observations is close to a calorimeter for CR electrons in order of magnitude, the superlinear slopes of the L_{radio}–SFR and L_{radio}–$\dot{E}_{SN(Ia+CC)}$ relations (at least in *L* band) are inconsistent with the calorimeter model for the disc. Instead, the superlinearity could be naturally reproduced with equipartition non-calorimeter models. These non-calorimeter models predict a strong dependence of the non-thermal radio emission on the magnetic field strength, which depends on the SFR. In addition to a higher radio radiation efficiency, the X-ray radiation efficiency may also slightly decrease in intense star-forming galaxies (Li & Wang 2013b; Wang et al. 2015), helping to produce the sublinear L_X–L_{radio} slopes.

The superlinear radio–IR relation indicates that high-SFR galaxies are closer to calorimeter conditions. This scenario also predicts that the galaxies are better calorimeters for higher energy electrons because their energy loss via synchrotron radiation is faster than for lower energy electrons. Therefore, there should be a flatter radio–IR relation at higher frequencies. Such a trend is revealed by our results in *C* and *L* bands, but we could not further confirm it by comparing with archival observations, mainly because of the large diversity in various archival observations. Furthermore, different radio–IR slopes in *C* and *L* bands also predict a weak dependence of the integrated radio spectral index α on the SFR, which is indicated by the weak correlation between them, but the large scatter prevents us from further constraining a well-defined α–SFR relation. Future observations in broader bands with comparable quality to the CHANG-ES programme are needed to confirm the change of the radio–IR slope with the frequency of the radio continuum emission.

REFERENCES

Argo M. K., van Bemmel I. M., Connolly S. D., Beswick R. J., 2015, MNRAS, 452, 1081

Basu A., Roy S., 2013, MNRAS, 433, 1675

Basu A., Beck R., Schmidt P., Roy S., 2015a, MNRAS, 449, 3879

Basu A., Wadadekar Y., Beelen A., Singh V., Archana K. N., Sirothia S., Ishwara-Chandra C. H., 2015b, ApJ, 803, 51

Beck R., Wielebinski R., 2013, in Oswalt T. D., Gilmore G., eds, Planets, Stars and Stellar Systems, Vol. 5. Springer, New York, p. 641

Bell E. F., 2003, ApJ, 586, 794

Bell E. F., de Jong R. S., 2001, ApJ, 550, 212

Berkhuijsen E. M., Beck R., Tabatabaei F. S., 2013, MNRAS, 435, 1598

Calzetti D. et al., 2007, ApJ, 666, 870

Calzetti D. et al., 2010, ApJ, 714, 1256

Chevalier R. A., Clegg A. W., 1985, Nature, 317, 44

Chi X., Wolfendale A. W., 1990, MNRAS, 245, 101

Chyży K. T., Bomans D. J., Krause M., Beck R., Soida M., Urbanik M., 2007, A&A, 462, 933

Combes F., Braine J., Casoli F., Gerin M., van Driel W., 1992, A&A, 259, 65

Condon J. J., Cotton W. D., Broderick J. J., 2002, AJ, 124, 675

de Jong T., Klein U., Wielebinski R., Wunderlich E., 1985, A&A, 147, L6

Dickey J. M., Salpeter E. E., 1984, ApJ, 284, 461

Domingo-Santamaría E., Torres D. F., 2005, A&A, 444, 403

Dumke M., Krause M., Wielebinski R., 2000, A&A, 355, 512

Ehlert S., Werner N., Simionescu A., Allen S. W., Kenney J. D. P., Million E. T., Finoguenov A., 2013, MNRAS, 430, 2401

English J., Irwin J. A., 1997, AJ, 113, 2006

Everett J. E., Zweibel E. G., Benjamin R. A., McCammon D., Rocks L., Gallagher J. S., III, 2008, ApJ, 674, 258

Fullmer L., Lonsdale C. J., 1989, Cataloged Galaxies and Quasars Observed in the IRAS Survey, Version 2. Jet Propulsion Laboratory, Pasadena, CA

Gallimore J. F., Axon D. J., O'Dea C. P., Baum S. A., Pedlar A., 2006, AJ, 132, 546

Green D. A., 2014, Bull. Astron. Soc. India, 42, 47

Gregory P. C., Condon J. J., 1991, ApJS, 75, 1011

Hada K., Doi A., Nagai H., Inoue M., Honma M., Giroletti M., Giovannini G., 2013, ApJ, 779, 6

Heald G. et al., 2011, A&A, 526, 118

Heckman T. M., Armus L., Miley G. K., 1990, ApJS, 74, 833

Heesen V., Brinks E., Leroy A. K., Heald G., Braun R., Bigiel F., Beck R., 2014, AJ, 147, 103

Heesen V. et al., 2015, MNRAS, 447, 1

Helou G., Soifer B. T., Rowan-Robinson M., 1985, ApJ, 298, L7

Hoopes C. G., Walterbos R. A. M., Rand R. J., 1999, ApJ, 522, 669

Hopkins P. F., Quataert E., Murray N., 2012, MNRAS, 421, 3522

Hummel E., Saikia D. J., 1991, A&A, 249, 43

Irwin J. A. et al., 2012a, AJ, 144, 43

Irwin J. A. et al., 2012b, AJ, 144, 44

Irwin J. A. et al., 2013a, AJ, 146, 164

Irwin J. A., Brar R. S., Saikia D. J., Henriksen R. N., 2013b, MNRAS, 433, 2958

Irwin J. A., Henriksen R. N., Krause M., Wang Q. D., Wiegert T., Murphy E. J., Heald G., Perlman E., 2015, ApJ, 809, 172

Jarrett T. H. et al., 2013, AJ, 145, 6

Kenney J. D. P., Tal T., Crowl H. H., Feldmeier J., Jacoby G. H., 2008, ApJ, 687, L69

Kennicutt R. C., 1998, ARA&A, 36, 189

Kennicutt R. C., Evans N. J., 2012, ARA&A, 50, 531

Kosenko D., Ferrand G., Decourchelle A., 2014, MNRAS, 443, 1390

Krause M., 2009, Rev. Mex. Astron. Astrofis., 36, 25

Krause M., 2011, in Soida M., Otmianowska-Mazur K., de Gouveia Dal Pino E. M., Lazarian A., eds, Proc. of Magnetic Fields in the Universe III: From Laboratory and Stars to Primordial Structures, Zakopane, Poland, preprint (arXiv:1111.7081)

Krause M., Wielebinski R., Dumke M., 2006, A&A, 448, 133

Lacki B. C., Thompson T. A., Quataert E., 2010, ApJ, 717, 1

Li J.-T., 2015, MNRAS, 453, 1062

Li J.-T., Wang Q. D., 2013a, MNRAS, 428, 2085

Li J.-T., Wang Q. D., 2013b, MNRAS, 435, 3071

Li J.-T., Li Z., Wang Q. D., Irwin J. A., Rossa J., 2008, MNRAS, 390, 59

Li J.-T., Wang Q. D., Li Z., Chen Y., 2009, ApJ, 706, 693

Li Z. et al., 2011, ApJ, 730, 84

Li J.-T., Wang Q. D., Li Z., Chen Y., 2011, ApJ, 737, 41

Li J.-T., Crain R. A., Wang Q. D., 2014, MNRAS, 440, 859

Lisenfeld U., Völk H. J., 2000, A&A, 354, 423

McMillan P. J., 2011, MNRAS, 414, 2446

Machacek M. E., Jones C., Forman W. R., 2004, ApJ, 610, 183

Makarov D., Prugniel P., Terekhova N., Courtois H., Vauglin I., 2014, A&A, 570, 13

Mannucci F., Della Valle M., Panagia N., Cappellaro E., Cresci G., Maiolino R., Petrosian A., Turatto M., 2005, A&A, 433, 807

Mora S. C., Krause M., 2013, A&A, 560, 42

Murphy E. J. et al., 2006, ApJ, 638, 157

Murphy E. J., Helou G., Kenney J. D. P., Armus L., Braun R., 2008, ApJ, 678, 828

Murphy E. J., Kenney J. D. P., Helou G., Chung A., Howell J. H., 2009, ApJ, 694, 1435

Murphy E. J. et al., 2011, ApJ, 737, 67

Niklas S., 1997, A&A, 322, 29

Niklas S., Beck R., 1997, A&A, 320, 54

Orlando E., Strong A., 2013, MNRAS, 436, 2127

Parizot E., 2014, Nucl. Phys. B, 256, 197

Parizot E., Marcowith A., van der Swaluw E., Bykov A. M., Tatischeff V., 2004, A&A, 424, 747

Price R., Duric N., 1992, ApJ, 401, 81

Rieke G. H., Alonso-Herrero A., Weiner B. J., Pérez-González P. G., Blaylock M., Donley J. L., Marcillac D., 2009, ApJ, 692, 556

Robitaille T. P., Whitney B. A., 2010, ApJ, 710, L11

Sanders D. B., Mazzarella J. M., Kim D.-C., Surace J. A., Soifer B. T., 2003, AJ, 126, 1607

Skrutskie M. F. et al., 2006, AJ, 131, 1163

Snowden S. L. et al., 1997, ApJ, 485, 125

Somerville R. S., Davé R., 2015, ARA&A, 53, 51

Stil J. M., Krause M., Beck R., Taylor A. R., 2009, ApJ, 693, 1392

Strickland D. K., Heckman T. M., 2007, ApJ, 658, 258

Strickland D. K., Heckman T. M., 2009, ApJ, 697, 2030

Strickland D. K., Stevens I. R., 2000, MNRAS, 314, 511

Strickland D. K., Heckman T. M., Weaver K. A., Hoopes C. G., Dahlem M., 2002, ApJ, 568, 689

Strickland D. K., Heckman T. M., Colbert E. J. M., Hoopes C. G., Weaver K. A., 2004, ApJ, 606, 829

Strong A. W., Moskalenko I. V., Ptuskin V. S., 2007, Annu. Rev. Nucl. Part. Syst., 57, 285

Strong A. W., Porter T. A., Digel S. W., Jóhannesson G., Martin P., Moskalenko I. V., Murphy E. J., Orlando E., 2010, ApJ, 722, L58

Strong A. W., Orlando E., Jaffe T. R., 2011, A&A, 534, 54

Tabatabaei F. S., Beck R., Krügel E., Krause M., Berkhuijsen E. M., Gordon K. D., Menten K. M., 2007, A&A, 475, 133

Temi P., Brighenti F., Mathews W. G., 2009, ApJ, 695, 1

Thompson T. A., Quataert E., Waxman E., Murray N., Martin C. L., 2006, ApJ, 645, 186

Tüllmann R., Breitschwerdt D., Rossa J., Pietsch W., Dettmar R.-J., 2006, A&A, 457, 779

Vlahakis C., Eales S., Dunne L., 2007, MNRAS, 379, 1042

Völk H. J., 1989, A&A, 218, 67

Wang Q. D., 2010, Publ. Natl. Acad. Sci., 107, 7168

Wang Q. D., Li J., Jiang X., Fang T., 2015, MNRAS, preprint (arXiv:1512.02655)

Werk J. K., Prochaska J. X., Thom C., Tumlinson J., Tripp T. M., O'Meara J. M., Peeples M. S., 2013, ApJS, 204, 17

Wiegert T. et al., 2015, AJ, 150, 81

Xu C., Lisenfeld U., Völk H. J., Wunderlich E., 1994, A&A, 282, 19

Yun M. S., Reddy N. A., Condon J. J., 2001, ApJ, 554, 803

Zhang D., Thompson T. A., Murray N., Quataert E., 2014, ApJ, 784, 93

Zhang S., Wang Q. D., Ji L., Smith R. K., Foster A. R., Zhou X., 2014, ApJ, 794, 61

Zhu Y.-N., Wu H., Li H.-N., Cao C., 2010, Res. Astron. Astrophys., 10, 329

This paper has been typeset from a TEX/LATEX file prepared by the author.